NRC Publications Archive
Archives des publications du CNRC

Design and use of spires for natural wind simulation

Irwin, H. P. A. H.

For the publisher's version, please access the DOI link below./ Pour consulter la version de l'éditeur, utilisez le lien DOI ci-dessous.

Publisher's version / Version de l'éditeur:
https://doi.org/10.4224/40002044
Laboratory Technical Report (National Research Council of Canada. National Aeronautical Establishment. Low Speed Aerodynamics Laboratory); no. LTR-LA-233, 1979-08

NRC Publications Archive Record / Notice des Archives des publications du CNRC :
https://nrc-publications.canada.ca/eng/view/object/?id=480e82aa-8dcf-4cd3-9d7b-9cb271d6cf2a
https://publications-cnrc.canada.ca/fra/voir/objet/?id=480e82aa-8dcf-4cd3-9d7b-9cb271d6cf2a

Access and use of this website and the material on it are subject to the Terms and Conditions set forth at
https://nrc-publications.canada.ca/eng/copyright
READ THESE TERMS AND CONDITIONS CAREFULLY BEFORE USING THIS WEBSITE.

L'accès à ce site Web et l'utilisation de son contenu sont assujettis aux conditions présentées dans le site
https://publications-cnrc.canada.ca/fra/droits
LISEZ CES CONDITIONS ATTENTIVEMENT AVANT D'UTILISER CE SITE WEB.

Questions? Contact the NRC Publications Archive team at PublicationsArchive-ArchivesPublications@nrc-cnrc.gc.ca. If you wish to email the authors directly, please see the first page of the publication for their contact information.

Vous avez des questions? Nous pouvons vous aider. Pour communiquer directement avec un auteur, consultez la première page de la revue dans laquelle son article a été publié afin de trouver ses coordonnées. Si vous n'arrivez pas à les repérer, communiquez avec nous à PublicationsArchive-ArchivesPublications@nrc-cnrc.gc.ca.

National Research Council Canada
Conseil national de recherches Canada

National Research Council Canada
Conseil national de recherches Canada

NATIONAL AERONAUTICAL ESTABLISHMENT

LABORATORY TECHNICAL REPORT

LTR - LA - 233

DESIGN AND USE OF SPIRES FOR NATURAL WIND STIMULATION

H.P.A.H. IRWIN

RAPPORT TECHNIQUE DE LABORATOIRE

ÉTABLISSEMENT AÉRONAUTIQUE NATIONAL

AUGUST 1979
OTTAWA, CANADA

National Research Council Canada
Conseil national de recherches Canada

NATIONAL AERONAUTICAL ESTABLISHMENT

ÉTABLISSEMENT AÉRONAUTIQUE NATIONAL

PAGES
PAGES 37

FIG.
DIAG. 25

TABLES
TABLES

REPORT
RAPPORT

LABORATORY / LABORATOIRE

REPORT
RAPPORT LTR-LA-233

DATE
DATE August 1979

LAB. ORDER
COMM. LAB.

FILE
DOSSIER

FOR
POUR

REFERENCE
RÉFÉRENCE

LTR - LA-233

DESIGN AND USE OF SPIRES FOR NATURAL WIND SIMULATION

SUBMITTED BY
PRÉSENTÉ PAR R. J. Templin
LABORATORY HEAD
CHEF DE LABORATOIRE

AUTHOR
AUTEUR H.P.A.H. Irwin

APPROVED
APPROUVÉ F. R. Thurston
DIRECTOR
DIRECTEUR

FORM
FORMULAIRE B

COPY NO.
COPIE NR.

5172413

SUMMARY

The status of the spire-roughness technique for planetary boundary layer simulation is briefly reviewed. The last report on the subject was in 1972 and since then the technique has been applied to a wider range of boundary layers and a much greater body of data has been accumulated. A design method is given with particular emphasis on triangular spires which it is suggested are as good as those of more complicated geometry. Results of spire drag measurements are described with due attention to blockage and interference effects. Finally, results from a number of spire generated boundary layers are collected together and compared with full scale data.

CONTENTS

Page

NOTATION

A	cross-sectional of the working section
A_S	total frontal area of the spires
b	base length of a triangular spire
C_D	measured drag coefficient
C_{D_O}	true drag coefficient including aerodynamic interference from adjacent spires
C_{D_∞}	true drag coefficient of an isolated spire
C_f	floor friction coefficient
c	$\kappa/(1+\kappa)$
d	width of working section
F_I	interference factor, C_{D_O}/C_{D_∞}
H	height of working section
H_E	$H(1 - 2w^2/Hd)$
h	height of spire
L_u^x, L_w^x	integral scales, defined as the area under the correlation curves for u and w respectively in the x direction
L_u^y, L_w^y	integral scales, defined as the area under the correlation curves for u and w respectively in the y direction
N	number of spires
p	static pressure
r	height of ramp
U	mean wind speed
$\overline{U}$	U averaged with respect to height
u, w	longitudinal and vertical turbulence velocities; w is also

	used for the fillet width in Section 2.5
u', w'	root-mean-square values of u and w respectively
x_o	distance downstream of the spires
x, y, z	along wind, across wind and vertical coordinates respectively
α	power law exponent, Equation 1
β	$\frac{\delta}{H}\frac{\alpha}{1+\alpha}$
β_E	$\frac{\delta_E}{H_E}\frac{\alpha}{1+\alpha}$
δy	distance between spire centre lines
δ	boundary layer thickness
δ_E	$(1 - w^2/\delta d)$
δ^*	displacement thickness
η	U_B/U_{B_e}
θ	blockage factor
κ	pressure drop coefficient $(p_A - p_B)/(\frac{1}{2}\rho U_{Ae})$
ρ	air density
ψ	Equation 19

Subscripts

1, 2, 3	station numbers, Figure 3
A,B	station letters, Figure 7
e	external to boundary layer

INTRODUCTION

The initial work of the Low Speed Aerodynamics Laboratory on methods of artificially generating thick boundary layers that simulate the planetary boundary layer began in 1968 and is described by Templin(1). The object was to generate a thick boundary layer without having a long upwind fetch, thereby enabling the full potential of aeronautical wind tunnels to be realized for wind engineering work, despite the low length to height ratios of their working sections. Further developments and the emergence of the spire-roughness technique are described by Campbell and Standen(2), and Standen(3), the last report being written in 1972. Since then a large number of wind engineering projects have been carried out using the spire-roughness technique and the method has also been adopted by other laboratories. An example of the use of the technique in the N.A.E. 9m × 9m wind tunnel is shown in Figure 1. It has enabled simulated boundary layers up to 4m thick to be generated.

The original method used by Campbell and Standen(2) to design the shape of the spires was an adaptation of Cowdrey's method(4) for the design of grids. It centred around the form of the desired wind velocity profile

$$\frac{U}{U_e} = \left(\frac{z}{\delta}\right)^{\alpha} \tag{1}$$

where U = mean (time averaged) wind velocity profile

U_e = value of U above the boundary layer

z = height above the wind tunnel floor

δ = thickness of boundary layer

α = a constant in the range 0.1 to 0.5

The spire shape was simply designed for a particular value of α and to give acceptable lateral uniformity of the mean velocity profile at a distance approximately six spire heights downstream of the spires. No considerations of the turbulence intensity or length scale entered into the calculation of the spire shape. Despite this, the spires were successful in giving a fair simulation of the turbulence in a neutral planetary boundary layer with the same mean velocity profile as that produced by the spires and roughness.

Experience since 1972 with a wide range of boundary layer simulations, some of which is described in this report, has repeatedly confirmed the success of the spire-roughness technique. However, a consistent finding has been that Campbell and Standen's method of calculating the spire shape required some improvement. The resulting spire drag was too high, producing a boundary layer with too high a value of α and with turbulence properties appropriate to the high α value. Thus, it became necessary to make ad-hoc modifications to the spire shape in the wind tunnel before an acceptable boundary layer simulation was finally obtained. An example of such an ad-hoc modification, made by Standen in Reference 3, is shown in Figure 2. Another finding from experience has been that any roughly triangular shaped spires will give an acceptable boundary layer simulation at six spire heights downstream provided they have the correct overall drag coefficient, are spaced laterally at intervals of approximately half a spire height and are combined with the correct floor roughness. In other words the fine details of the spire shape are not important. It appears that the vigorous mixing process that occurs just downstream of the spires rapidly obliterates the finer details of the spire imprint on the flow and, in the presence of the floor roughness, produces a velocity profile of approximately the power law form of its own accord.

In Section 2 of this report a new method of designing spires is described, based on considerations of overall momentum balance. Particular attention is given to spires that are triangular, since it appears unnecessary to go to more complex shapes. The empirical assumptions used are more directly applicable to spires than are those of Cowdrey's grid method and the effect of floor roughness is included. Some discussion of secondary effects such as fillets, ramps and blockage is also given. The design method is compared with some existing data on spire-roughness generated boundary layers in Section 3. Section 4 gives experimental results on the drag of and flow around triangular spires. Section 5 briefly reviews results from a number of past boundary layer simulations with power law exponents ranging from 0.1 to 0.5 and compares them with full scale data.

2. THEORY

2.1 Momentum Balance in a Rectangular Working Section

Figure 3 is a diagram of a wind tunnel rectangular working section the presence of fillets in the corners being, for the present, ignored. Stations 1, 2 and 3 are identified in Figure 3 as being upstream of the spires, at the spires and downstream of them respectively. The air velocity and static pressure are assumed to be uniform over the working section at Station 1. Often the spires are situated just at the entrance to the working section with the contraction immediately upstream, which will tend to result in some non-uniformity in the oncoming flow that is ignored here (and in Campbell and Standen's method) for simplicity. At Station 3, the static pressure is assumed to be uniform and the wind velocity uniform laterally, but not vertically because of the boundary layer of thickness δ on the working section floor. Treating the interior of the working section between Stations 1 and 3 as a control volume, the momentum balance can be written in words as

excess of momentum flux at Station 3 over that at Station 1 = force due to pressure drop from Station 1 to Station 3
- reaction force of the spires on the air
- frictional forces of the floor, walls and ceiling on the air

First, the nature of the frictional term will be briefly examined. The frictional forces on all surfaces other than the roughness covered area of the floor can reasonably be neglected. The size of the frictional force on the roughness covered area depends on, among other factors, the distance from

Station 2 to Station 3. In normal applications the wind tunnel model is at about six spire heights downstream of Station 2, it being found empirically that the mean velocity profile reaches a state of horizontal uniformity at approximately this distance from the spires. The distance, x_0, from Station 2 to Station 3 is therefore assumed to be of this order. The size of the friction force is then expressed as

$$\text{Friction Force} = \tfrac{1}{2}\rho U_e^2 C_f x_o d$$

where C_f = an effective surface friction coefficient

U_e = wind velocity above the boundary layer at Station 3

d = width of working section

ρ = air density

The problem of specifying a value of C_f will be discussed later.

The momentum balance equation can thus be expressed as

$$\rho d \int_o^H U_3^2 dz - \rho U_1^2 H d = (p_1 - p_3) H d - \tfrac{1}{2}\rho U_2^2 C_{D_o} A_s - \tfrac{1}{2}\rho U_e^2 C_f x_o d \qquad (2)$$

where number subscripts refer to Stations,

H = height of working section

p = static pressure

C_{D_o} = drag coefficient of each spire (based on frontal area) in the absence of blockage but including the aerodynamic interference of adjacent spires

and A_s = total frontal area of all the spires

The value of U_2 is influenced by blockage effects and is the velocity, commonly used for blockage corrections, of a fictitious uniform airflow, unconstrained by walls or ceiling, that would produce the same drag on the spires as exists when the walls and ceiling are present. The treatment of the spire drag is simpler in the present method than in Reference 2 where the strip assumption was used together with the assumption, implicit in Cowdrey's method, that the wind velocity immediately upstream of Station 2 is the same at any given height as at Station 3. The strip assumption is difficult to justify, because of the large scale, vigorous mixing that occurs downstream of the spires, and the second assumption, concerning the velocity profile just upstream of Station 2, does not compare well with measurements in the flow at the spire station described in Section 4.6. The continuity equation is

$$U_1 H = \int_0^H U_3 dz = \int_0^\delta U_3 dz + (H - \delta) U_e \qquad (3)$$

Since the power law, Equation 1, is assumed to apply in the boundary layer at Station 3, it can be deduced from Equation 3 that

$$\frac{U_e}{U_1} = \frac{1}{1 - \frac{\delta}{H} \frac{\alpha}{1+\alpha}} \qquad (4)$$

Above the boundary layer Bernoulli's equation is valid. Hence,

$$p_1 + \tfrac{1}{2}\rho U_1^2 = p_3 + \tfrac{1}{2}\rho U_e^2 \qquad (5)$$

Eliminating U_e from Equation 5 by use of Equation 4, and re-arranging,

$$\frac{p_1 - p_3}{\frac{1}{2}\rho U_1^2} = \left[\frac{1}{\left(1 - \frac{\delta}{H} \frac{\alpha}{1+\alpha}\right)^2} - 1 \right] \qquad (6)$$

Dividing Equation 2 by $\frac{1}{2}\rho U_1^2$ gives

$$2d\int_0^H \left(\frac{U_3}{U_1}\right)^2 dz - 2Hd = \frac{p_1 - p_3}{\frac{1}{2}\rho U_1^2} \cdot Hd - \left(\frac{U_2}{U_1}\right)^2 C_{D_o} A_s - \left(\frac{U_e}{U_1}\right)^2 C_f x_o d \qquad (7)$$

The first term on the left hand side can be expressed as

$$2d\int_0^H \left(\frac{U_3}{U_1}\right)^2 dz = 2d\left(\frac{U_e}{U_1}\right)^2 \int_0^H \left(\frac{U_3}{U_e}\right)^2 dz = 2d\left(\frac{U_e}{U_1}\right)^2 \left[\int_0^\delta \left(\frac{U_3}{U_e}\right)^2 dz + H - \delta\right]$$

which, from Equations 1 and 4, becomes

$$2d\int_0^H \left(\frac{U_3}{U_1}\right)^2 dz = 2Hd\,\frac{\left(1 - \frac{\delta}{H}\,\frac{2\alpha}{1+2\alpha}\right)}{\left(1 - \frac{\delta}{H}\,\frac{\alpha}{1+\alpha}\right)^2} \qquad (8)$$

Thus, using Equations 4, 6 and 8, Equation 7 can be written as

$$2Hd\,\frac{\left(1 - \frac{\delta}{H}\,\frac{2\alpha}{1+2\alpha}\right)}{\left(1 - \frac{\delta}{H}\,\frac{\alpha}{1+\alpha}\right)^2} - 2Hd = Hd\left(\frac{1}{\left(1 - \frac{\delta}{H}\,\frac{\alpha}{1+\alpha}\right)^2} - 1\right) - \left(\frac{U_2}{U_1}\right)^2 C_{D_o} A_s - \frac{1}{\left(1 - \frac{\delta}{H}\,\frac{\alpha}{1+\alpha}\right)^2}\, C_f x_o d \qquad (9)$$

from which it is deduced that the expression for A_s/Hd is

$$\frac{A_s}{Hd} = \left(\frac{U_1}{U_2}\right)^2 \frac{1}{C_{D_o}} \left(2\frac{\delta}{H}\,\frac{\alpha}{(1+\alpha)(1+2\alpha)} + \left(\frac{\delta}{H}\,\frac{\alpha}{1+\alpha}\right)^2 - C_f\,\frac{x_o}{H}\right) \Bigg/ \left(1 - \frac{\delta}{H}\,\frac{\alpha}{1+\alpha}\right)^2 \qquad (10)$$

It is necessary, at some stage, to determine the ratio U_2/U_1, which would be unity were it not for the blockage effect of the spires. To obtain $\frac{U_2}{U_1}$, Maskell's blockage correction$^{(5)}$ for bluff bodies will be used.

Maskell's correction can be expressed as

$$\left(\frac{U_2}{U_1}\right)^2 = 1 + \theta\left(\frac{U_2}{U_1}\right)^2 C_{D_O} \frac{A_S}{Hd}$$

which may be rearranged to give

$$\left(\frac{U_1}{U_2}\right)^2 = 1 - \theta C_{D_O} \frac{A_S}{Hd} \qquad (11)$$

where θ is the blockage factor, lying in the range 1.0 (for two dimensional bodies) to 2.8 (for bodies with aspect ratios near unity). Substituting, for $\frac{U_1}{U_2}$ in Equation 10 and rearranging, the following relation is arrived at,

$$A_s = \frac{\psi Hd}{(1+\psi\theta)C_{D_O}} \qquad (12)$$

where

$$\psi = \beta\left(\frac{2}{1+2\alpha} + \beta - C_f \frac{x_O}{\delta} \frac{1+\alpha}{\alpha}\right)\Big/(1-\beta)^2 \qquad (12a)$$

and

$$\beta = \frac{\delta}{H} \frac{\alpha}{1+\alpha}$$

Equation 12 is a relation that the total area, A_S, of the spires must obey if momentum is to be conserved, given that the downstream velocity distribution is of the assumed form, i.e. is laterally uniform and obeys the power law in the boundary layer. However, an arbitrary array of spires of area A_S will not necessarily produce the assumed velocity distribution and it requires additional relations, empirical in nature, to define the spire geometry completely.

2.2 Floor Friction Coefficient

The friction term in Equation 2 tends to be small in relation to the other terms for the range of x_o considered in this report. Thus the value of C_f does not have to be determined with great accuracy and the assumption that is adopted here is that C_f is equal to the local skin friction coefficient at Station 3. The floor roughness is assumed to have been chosen to be appropriate to the required values of α and δ using the available roughness correlations, such as that of Wooding, Bradley and Marshall(6) for example. Gartshore(7) gives the following approximate relation between the local skin friction coefficient, here identified with C_f, and α for boundary layers near equilibrium

$$C_f = 0.136\left(\frac{\alpha}{1+\alpha}\right)^2 \qquad (13)$$

Substitution of Equation 13 into the expression for ψ, Equation 12(a), leads to,

$$\psi = \beta\left(\frac{2}{1+2\alpha} + \beta - \frac{x_o}{\delta}\,\frac{0.136\alpha}{1+\alpha}\right)\Big/(1-\beta)^2 \qquad (14)$$

where again β stands for $\frac{\delta}{H}\,\frac{\alpha}{1+\alpha}$. The approximation involved in assuming that the boundary layer at Station 3 is near to equilibrium is acceptable in view of the level of accuracy required for C_f.

2.3 Design of Triangular Spires at Half-Height Spacing

For an array of N triangular spires of height, h, and base, b, it is deduced from Equation 12 that the required base to height ratio is given by

$$\frac{b}{h} = 2\frac{Hd}{Nh^2}\frac{\psi}{(1+\psi\theta)C_{D_O}} \tag{15}$$

where ψ is given by Equation 14. When the spire centre-lines are spaced laterally at intervals of $\frac{h}{2}$ and when, in addition, $\frac{h}{2}$ goes into d exactly N times, Equation 15 can be written

$$\frac{b}{h} = \frac{H}{h} \cdot \frac{\psi}{(1+\psi\theta)C_{D_O}} = \frac{\delta}{h} \cdot \frac{\psi H/\delta}{(1+\psi\theta)C_{D_O}} \tag{16}$$

There should usually be no difficulty in choosing the spire height such that $\frac{2d}{h}$ is an integer thereby ensuring that Equation 16 is applicable exactly. For example, in a square working section this gives a choice of $\frac{h}{H}$ from the values, $1, \frac{2}{3}, \frac{1}{2}, \frac{2}{5}, \frac{1}{3}, \frac{2}{7}, \frac{1}{4}, \frac{2}{9}, \frac{1}{5}, \frac{2}{11} \ldots \frac{2}{J} \ldots$, where J is an integer, and there is even less restriction for rectangular working sections where $\frac{d}{H} > 1$. In the interests of maintaining maximum lateral uniformity of the flow the spire array should ideally be positioned symmetrically in the working section. This results in the centres of the two end spires being a distance $\frac{h}{4}$ from the working section walls so that the image effect of the walls then effectively extends the array to infinity and the interference effects for the end spires are nominally the same as for the rest. When corner fillets are present some lateral non-uniformity of the flow is inevitable near the walls but there is still some merit in retaining the same spire arrangement as without the fillets, simply removing the area of the end spires that would occupy the space cut off by the fillets. In Section 2.5 the effects of fillets are discussed in more detail.

The empirical data required to make Equation 16 useful in calculating the spire shape are C_{D_o}, θ and $\frac{\delta}{h}$. In Section 4 drag measurements on arrays of three triangular spires are described yielding $C_{D_o} = 1.45$ and $\theta = 1.7$ for spires with shapes in the range $0.05 < \frac{b}{h} < 0.20$ at $\frac{1}{2}$h spacing. However, comparisons with experiment in Section 3 indicate θ may be as low as 1.0 for a full array mounted just downstream of a contraction. Experience with spires of various shapes, some of which were close to triangular, indicates that $\frac{\delta}{h}$ at $x_o \simeq 6h$ is slightly below unity and increases gradually as α increases. Figure 4 gives some data on $\frac{\delta}{h}$ from several wind simulations. The straight line

$$\frac{\delta}{h} = 0.72(1 + \tfrac{1}{2}\alpha) \tag{17}$$

has been drawn to represent the data and any dependence of $\frac{\delta}{h}$ on $\frac{\delta}{H}$ has been neglected. For the two points with flags the data were obtained at $x_o = 4.5$ h rather than 6 h and the experimental value of $\frac{\delta}{h}$ was increased by 2% to correct for a 2% area contraction caused by the presence of a ramp downstream of the spires. The value of δ for each wind simulation was determined as the height at which the power law that best fitted the velocity data reached the free stream velocity. Substituting, $C_{D_o} = 1.45$ and $\frac{\delta}{h} = 0.72(1 + \frac{1}{2}\alpha)$ into Equations 14 and 16 the following expressions for b/h and ψ are arrived at

$$\frac{b}{h} = 0.497\,\frac{\psi H/\delta}{1 + \theta\psi}(1 + \tfrac{1}{2}\alpha) \tag{18}$$

$$\psi = \beta\left(\frac{2}{1 + 2\alpha} + \beta - \frac{x_o}{h}\,\frac{0.188\alpha}{(1 + \alpha)(1 + \frac{1}{2}\alpha)}\right) / (1 - \beta)^2 \tag{19}$$

where $\beta = \frac{\delta}{H}\frac{\alpha}{1+\alpha}$ as before.

Equations 18 and 19 are the design formulae for triangular spires at $\frac{h}{2}$ spacing, with h preferably chosen such that $\frac{2d}{h}$ is an integer in order to obtain the closest approximation to an infinite array. Figure 5 shows $\frac{b}{h}$ plotted against α for a range of values of $\frac{\delta}{H}$ assuming $\frac{x_o}{h} = 6$. Results are given for $\theta = 1.0$ and 1.7. It can be seen that the value of α produced by the spires is predicted to be more sensitive to $\frac{b}{h}$ at the higher values of $\frac{b}{h}$. The effect of increasing $\frac{\delta}{H}$ is to increase the value of $\frac{b}{h}$ that is required to produce a given value of α. The reason for this increase in $\frac{b}{h}$ with $\frac{\delta}{H}$ is that the pressure drop coefficient, $\frac{p_1 - p_3}{\frac{1}{2}\rho U_1^2}$, increases as $\frac{\delta}{H}$ increases (see Equation 6). Since a greater pressure drop acts so as to decrease α, more spire drag is required in order to maintain α at a given value. Some of this comes from an increase in blockage but the balance must be supplied by an increase in b/h.

2.4 Size of the Floor Friction Effect

The effect of the floor friction is most easily seen in the simplified case where $\frac{\delta}{H}$ is very small. The expression, Equation 18, for $\frac{b}{h}$ then reduces to

$$\frac{b}{h} = 0.994\frac{(1+\frac{1}{2}\alpha)\alpha}{(1+\alpha)(1+2\alpha)}\left[1 - 0.56\frac{\alpha(1+2\alpha)}{(1+\alpha)(1+\frac{1}{2}\alpha)}\right] \qquad (20)$$

The effect of the floor friction is represented by the second term in the square parentheses and it can be seen that the floor friction reduces the required value of $\frac{b}{h}$. The percentage reduction is roughly proportional to α in the interesting range $0 < \alpha < 0.5$. For $\alpha = 0.25$ the calculated reduction in $\frac{b}{h}$ is 15%.

2.5 Effect of Corner Fillets

In Section 2.1 the overall momentum balance in an exactly rectangular working section was considered. The same considerations can be applied to rectangular working sections with corner fillets, provided some assumptions are made concerning the velocity profile over the fillets. The effect of the fillets is generally small thus justifying the use of fairly crude assumptions for the velocity over the fillets. With 45 degree triangular fillets, intersecting the walls, floor and ceiling at a distance w from the corners, the cross-sectional area of the working section, A, is reduced to

$$A = Hd - 2w^2 \tag{21}$$

and the momentum equation becomes

$$\rho\iint_A U_3^2 dA - \rho U_1^2 A = (p_1 - p_3)A - \tfrac{1}{2}\rho U_2^2 C_{D_O} A_s - \tfrac{1}{2}\rho U_e^2 C_f x_o (d - 2w) \tag{22}$$

In the frictional term on the right hand side it has been assumed that the fillets have no roughness. The continuity equation is

$$U_1 A = \iint_A U_3 dA \tag{23}$$

The assumption that is now made concerning the vertical profile of velocity over the fillets at Station 3 is that the same power law, Equation 1, is maintained as elsewhere but that the boundary layer vertical depth is locally compressed in such a way that the top of the boundary layer remains level with the top of the boundary layer in the central part of the working section. The algebraic details will be omitted here but the resulting expression for A_s, after carrying out the area integrations in Equations 22 and 23, can be written in the form

$$A_s = \frac{\psi H_E d}{(1+\psi\theta)\, C_{D_0}} \tag{24}$$

$$\text{where } \psi = \beta_E\left(\frac{2}{1+2\alpha} + \beta_E - C_f \frac{x_0}{\delta_E}\,\frac{\alpha+1}{\alpha}\left(1-\frac{2w}{d}\right)\right)\Bigg/\left(1-\beta_E\right)^2 \tag{24a}$$

$$\left.\begin{aligned} \beta_E &= \frac{\delta_E}{H_E}\,\frac{\alpha}{1+\alpha} \\ \delta_E &= \delta\left(1-\frac{w^2}{\delta d}\right) \\ H_E &= H\left(1-\frac{2w^2}{Hd}\right) \end{aligned}\right\} \tag{25}$$

In deriving these results it was assumed that $\delta \geq w$. Equations 24 and 24(a) are identical to Equations 12 and 12(a), except that in place of δ and H there are now the 'effective' values, δ_E and H_E, defined by Equations 25. In addition the factor $1 - \frac{2w}{d}$ multiplying the skin friction term enters into the expression for ψ because of the assumption that the fillets have no roughness.

Figure 6 shows the percentage change in $\frac{A_s}{Hd}$ that is required according to Equation 24 in changing the fillet dimension from $w = 0$ to $w = 0.1\ H$ in a square working section. The values of C_f, C_D and $\frac{x_o}{h}$ that were used were the same as in Sections 2.2 and 2.3 and θ was assumed to be 1.7. It can be seen from Figure 6 that the effect of the corner fillets is small (less than 4%) for $\delta/w > 3$. For $\delta/w < 3$ the required value of $\frac{A_s}{Hd}$ drops off due to the fact that the area of working section occupied by the boundary layer suffers a significant percentage reduction because part of it is cut off by the fillets, implying that less momentum need be taken out of the flow by the spires. The slight enlargement of $\frac{A_s}{Hd}$ at high values of δ/w is required to overcome the effect of an increased pressure drop across the spires which is the consequence of the reduced working section area.

Considering the practical aspects, and using the approximate analysis of this section as a guide rather than as giving an exact correction for the fillets, the simplest procedure in dealing with fillets is to use the same spire arrangement as without fillets, allowing the fillets to cut off the spire areas that fall under them. At high values of δ/w the spire areas lost will be negligible and, from Figure 5, very little change in A_s is in fact required. At low values of δ/w some reduction in A_s is desirable in the fillet regions and this will be approximately provided by the cutting off of the base areas of the end spires by the fillets.

2.6 Effect of a Ramp

Sometimes a ramp is present on the wind tunnel floor between the spires and the model. This introduces a pressure drop and a contraction of the streamlines and it is desirable to have an estimate of the effects on the boundary layer simulation. An approximate analysis is given in this Section in which it is assumed that the effect of the ramp is similar to the effect of a sudden drop in static pressure on a boundary layer. If the drop in pressure is sudden enough the shear stresses in the flow can be ignored and the assumption made that the total head is conserved along a mean streamline. The analysis is based on that given by Cowdrey in Reference 8 but more detailed results are given here.

Figure 7 defines two Stations, A and B, upstream and downstream of the ramp respectively, the ramp height being r. The pressure drops as the flow passes over the ramp due to the area contraction, but also the floor boundary layer displacement thickness, δ^*, is reduced so the pressure drop is not as large as if there were no floor boundary layer. The pressure drop coefficient is defined as

$$\kappa = \frac{p_A - p_B}{\frac{1}{2}\rho U_{Ae}^2} \qquad (26)$$

where subscripts A and B denote the Stations A and B and U_{Ae} is the velocity at Station A external to the boundary layer. For the moment it will be assumed that it is κ that is specified rather than the ramp height. Later, the relation between κ and r will be established. Since total head is assumed to be conserved, Bemoulli's equation applies along a streamline. Thus, even inside the boundary layer,

$$p_B + \tfrac{1}{2}\rho U_B^2 \quad = \quad p_A + \tfrac{1}{2}\rho U_A^2$$

on a streamline, which results in

$$U_B \quad = \quad \sqrt{\kappa U_{Ae}^2 + U_A^2} \tag{27}$$

Outside the boundary layer

$$U_{Be} \quad = \quad U_{Ae}\sqrt{\kappa + 1} \tag{28}$$

Equation 27 gives U_B but the height of the streamline at Station B needs to be found before the modified velocity profile can be calculated. This can be obtained from the continuity expression

$$U_B dz_B \quad = \quad U_A dz_A \tag{29}$$

where dz_A and dz_B are infinitesimal height differences separating the same two streamlines at Stations A and B respectively. At Station A the velocity profile obeys the power law, Equation 1, from which it is deduced that

$$dz_A \quad = \quad \frac{\delta_A}{\alpha}\left(\frac{U_A}{U_{Ae}}\right)^{\frac{1}{\alpha} - 1} d(U_A/U_{Ae}) \tag{30}$$

Eliminating U_A and U_{Ae}, using Equations 27 and 28, and substituting Equation 30 into Equation 29

$$dz_B \quad = \quad \frac{\delta_A}{\alpha}(1 + \kappa)^{\frac{1}{2\alpha}} \left[\left(\frac{U_B}{U_{Be}}\right)^2 - \frac{\kappa}{1 + \kappa}\right]^{\frac{1 - \alpha}{2\alpha}} d(U_B/U_{Be}) \tag{31}$$

The integration of Equation 31 gives the height of the streamline at Station B in terms of (U_B/U_{Be}). The resulting expression is in fact the velocity profile at Station B in an inverse form. The integration is most easily carried out when $\frac{1}{\alpha}$ is equal to an odd integer and the resulting inverse expressions for the velocity profile are,

$$\left.\begin{aligned}
&\text{for } \alpha = \tfrac{1}{3}, \\
&\qquad z_B = \delta_A(1+\kappa)^{3/2} \cdot (\eta^3 - 3c\eta + 2c^{3/2}) \\
&\text{for } \alpha = \tfrac{1}{5}, \\
&\qquad z_B = \delta_A(1+\kappa)^{5/2}(\eta^5 - \tfrac{10}{3}c\eta^3 + 5c^2\eta - \tfrac{8}{3}c^{5/2}) \\
&\text{and for } \alpha = \tfrac{1}{7} \\
&\qquad z_B = \delta_A(1+\kappa)^{7/2}(\eta^7 - \tfrac{21}{5}c\eta^5 + 7c^2\eta^3 - 7c^3\eta + \tfrac{16}{5}c^{7/2}),
\end{aligned}\right\} \quad (32)$$

where $\eta = \frac{U_B}{U_{Be}}$ and $c = \frac{\kappa}{1+\kappa}$. It can be seen that the velocity profile at Station B is no longer strictly of power law form. From Equations 27 and 28 there is a slip velocity at the floor equal to $U_{Be}\sqrt{c}$ which is clearly unrealistic. In reality high shear stresses are generated by such a discontinuity at the floor and they alter the velocity profile near to the floor so that it still obeys the no-slip condition. However, in the outer part of the boundary layer Equations 32 give a guide as to the effect of a ramp.

To find the relation between κ and r it is deduced from continuity and Equation 28 that

$$(H - r - \delta_B^*)\sqrt{\kappa + 1} = H - \delta_A^* \qquad (33)$$

where $\delta^* = \int_0^{\delta} (1 - \frac{U}{U_e}) dz$. Hence the expression for $\frac{r}{H}$ in terms of κ is

$$\frac{r}{H} = 1 - \frac{\delta_B^*}{\delta_A} \cdot \frac{\delta_A}{H} - \left(1 - \frac{\delta_A^*}{\delta_A} \cdot \frac{\delta_A}{H}\right) \Big/ \sqrt{1 + \kappa} \qquad (34)$$

The value of δ_A/H is known, the value of $\frac{\delta_A^*}{\delta_A}$ is $\frac{\alpha}{1 + \alpha}$, from Equation 1, and $\frac{\delta_B^*}{\delta_A}$ can be obtained by numerical integration of the velocity profile at Station B, as given by Equations 32, once κ has been specified. Thus, $\frac{r}{H}$ was evaluated for a number of values of κ and $\frac{\delta_A}{H}$ and the results are plotted in Figure 8. This Figure can be regarded as giving κ as a function of $\frac{r}{H}$ for different upstream boundary layers.

Using Figure 8 and Equations 32 the effect of a ramp of height 0.1 H has been calculated and the change in the velocity profile is illustrated in Figure 9 for initial boundary layers with $\alpha = 1/3$, 1/5 and 1/7 and $\delta_A = 0.3H$. A ramp of this size causes significant departures from the initial velocity profile. Departures of similar magnitude can be expected when the area contraction is due to model blockage rather than a ramp.

3.0 COMPARISON WITH EXPERIMENTAL DATA

References 9 to 12 describe three projects involving application of the spire roughness technique. The projects were on the Olympic Stadium in Montreal, the Commerce Court Tower in Toronto and the Lions'

Gate Bridge in Vancouver, and, together with Standen's development work in Reference 3, cover the range of boundary layers for very smooth terrain ($\alpha = 0.1$) to very rough terrain ($\alpha = 0.5$). Since several different approaches to designing the spires were used, the present method not included, the spire shapes did not belong to a single family, some being nearly triangular, others being flared near the base or having cut outs. It is of interest to see how closely these various spires, and the boundary layers they produced, conformed to Equation 12, disregarding the detailed differences of shape. Figure 10 compares the experimental data with Equation 12 in which C_D was taken to be 1.45 and θ was given the three successive values 1.7 , 1.0 and 0. Solid symbols in the graph denote cases where the spires were triangular or very nearly so. In calculating the experimental values of ψ Equation 13 was used to give C_f. The experimental values of $\frac{A_s}{Hd}$ were calculated as though the spire array were infinite, ignoring the fact that in some of the experiments $\frac{2d}{h}$ was not an integer. It can be seen in Figure 10 that the data are in quite good agreement with the curve for $\theta = 1.7$, the value obtained in the blockage measurements of Section 4, but better agreement with the two highest points, one of which was for triangular spires, is obtained with $\theta = 1.0$. The blockage data in Section 4 were obtained at approximately one working-section height downstream of the contraction whereas the data in Figure 10 were with the spires at the exit plane of the contraction. The proximity of the contraction may explain the lower value of θ but more data points at high $\frac{A_s}{Hd}$ would be desirable.

In the following table values of b/h, calculated from Equation 18 using experimental values of α, $\frac{h}{H}$ and $\frac{x_o}{h}$ and assuming $\theta = 1.0$, are compared with the effective $\frac{b}{H}$ values actually used in several different wind simulations. Not all the spires were triangular. For non-triangular spires the effective value of b was taken to be the base of the triangle with the same area and height as the spire.

Related Reference	Spires Triangular or nearly so	α	$\frac{h}{H}$	$\frac{x_o}{h}$	Effective b/h in Experiments	b/h from Eqn 18. $\theta = 1.0$
13	Yes	0.10	0.30	6.0	0.076	0.076
12	No	0.16	0.30	6.0	0.101	0.106
10	Yes	0.23	0.50	4.5	0.146	0.142
10	No	0.25	0.50	4.5	0.156	0.149
11	Yes	0.38	0.233	6.0	0.143	0.160
11	Yes	0.42	0.233	6.0	0.161	0.166
3	No	0.53	0.167	6.0	0.184	0.166

Since the value $\theta = 1.0$ and the expression $\frac{\delta}{h} = 0.72(1 + \frac{1}{2}\alpha)$, used in Equation 18, were based on data from some of the boundary layers in the table, the comparison is not an entirely independent assessment of the accuracy of Equation 18. However, the table does show that the differences between the calculated and experimental values of b/h are not large or systematic. The differences may be partly due to the spires being not strictly triangular in all cases or to the floor roughness being not quite appropriate to the boundary layer. No consistent method was used in designing the floor roughness.

It is suggested from the results of this Section that Equation

18 provides a sound basis for the design of spires and, as more data becomes available, it should be possible to determine the value of θ with more certainty. On the basis of the existing data θ is taken to be 1.0.

4. MEASUREMENTS OF DRAG ON TRIANGULAR SPIRES

4.1 Scope of Experiments

To obtain the drag coefficient for triangular spires some measurements were made in the N.A.E. 1.83 m × 2.74 m wind tunnel during a three day period in June 1978. In addition some hot wire measurements were made in the flow in the vicinity of the spires, and smoke was introduced to make the flow patterns visible. Several factors were examined in the drag measurements, the aerodynamic interference of adjacent spires, the size of the blockage effect, the influence of the upstream floor boundary layer, the influence of $\frac{b}{h}$ and the effect of a splitter plate. Because of the brief nature of the experiments they were not exhaustive but the results provided the most essential data required by the theory of Section 2. The spires, made from 1.58 mm thick steel, had a triangular splitter plate as shown in Figure 11 except for the one case that is described where the effect of removing the splitter plate was examined. The experiments were run at a nominal wind speed of 62.5 m/s and the drag was measured using the wind tunnel balance. A few measurements at half wind speed revealed no discernable Reynolds number effect.

4.2 Interference Effect

The drag of a spire with h = 0.610 m and $\frac{b}{H}$ = 0.15 was measured with two identical spires positioned symmetrically on either side, the centre spire being in the centre of the working section. The lateral spacing, δy, of the spire centre lines was varied and the resulting plot of C_D versus $\frac{\delta y}{b}$, uncorrected for blockage or the upstream boundary layer, is shown in Figure 12(a). As can be seen, little change occurred in C_D between $\frac{\delta y}{b} = 10$ and $\frac{\delta y}{b} = 5$ but for spacings smaller than $\frac{\delta y}{b} = 5$ the drag coefficient increased to a maximum at $\frac{\delta y}{h} = 3$ and then fell sharply for further decreases in $\frac{\delta y}{h}$. No interference data were obtained for values of $\frac{b}{h}$ other than 0.15 nor was the effect of adding more spires investigated. Treating the value of C_D at $\frac{\delta y}{b} = 10$ as indistinguishable from the asymptotic value at $\frac{\delta y}{b} = \infty$ and dividing it into the C_D data obtained at smaller spacings the curve of Figure 12(b) is obtained, giving the factor, F_I, by which the drag coefficient of a spire is increased (or decreased) due to the interference of the adjacent spires.

4.3 Blockage and Floor Boundary Layer Effects

One method that is used to obtain the size of the blockage effect is to measure C_D on models of different sizes and attribute the increments in C_D observed on the larger models to the increased blockage. In the present experiments the spires were mounted 1.8 m downstream of the end of the contraction and the bases lay in the thin boundary layer on the tunnel floor. An increase in the spire size would not only have increased the blockage but also would presumably have reduced the influence of the floor boundary layer on C_D, the two effects being intermingled. To isolate the blockage effect the method of adding additional spires was used, it being assumed that the principle of superposition of blockage effects was valid. Gould$^{(13)}$ gives data supporting the superposition principle. Let C_D be the measured drag coefficient of a spire with none others present and let C_D' be the measured drag coefficient with two others present but at a spacing, $\frac{\delta y}{b}$, sufficiently large that interference is negligible. Using Maskell's blockage correction$^{(5)}$ and the superposition principle

$$C_D = C_{D_\infty}\left(1 + \theta C_D \frac{\frac{1}{2}hb}{A}\right) \qquad (35)$$

$$C_D' = C_{D_\infty}\left(1 + \theta C_D' \frac{\frac{3}{2}hb}{A}\right) \qquad (36)$$

where C_{D_∞} = drag coefficient unaffected by blockage or interference

and A = cross-sectional area of working section = 5.063m^2.

Eliminating C_{D_∞} from these equations it is found that

$$\theta = \frac{C_D' - C_D}{C_D C'_D} \cdot \frac{A}{hb} \qquad (37)$$

From measurements on spires with dimensions $h = 0.610\text{m}$, $\frac{b}{h} = 0.15$ and with $\frac{\delta y}{b} = 10$ the values $C_D = 1.370$ and $C_D' = 1.407$ were obtained, yielding $\theta = 1.74$. Similar measurements were carried out on spires with twice the linear dimensions but with $\frac{\delta h}{b}$ reduced to 5 because of lack of room in the working section. In this case the measured value of C_D' was affected by interference. Thus, C_{D_∞} in Equation 36 was replaced by the modified drag coefficient, C_{D_o}, it being assumed that the interference effect was the same on all three spires. The blockage factor expression thus became

$$\theta = \frac{C'_D - C_D F_1}{C_D {C'_D}^{\frac{1}{2}}(3F_1 - 1)} \cdot \frac{A}{Hb} \qquad (38)$$

where $F_1 = \frac{C_{D_o}}{C_{D_\infty}}$ and is given by Figure 12(b) as 1.043 for $\frac{\delta y}{b} = 5$. Substitution of the measured values for the larger spires, $C_D = 1.433$ and $C'_D = 1.681$, in Equation 38 gave $\theta = 1.65$, in good agreement with the value deduced from the smaller spires. From these results the value of θ was taken to be 1.7.

The effect of blockage on the measurements of tunnel speed was not investigated experimentally. The speed was measured using two pressure taps in the contraction, the downstream tap being 2.2 m upstream of the station where the spires were mounted. Gould's data(13) indicate that the blockage effect this far upstream would have been less than 10% of the effect at the spire station.

To assess the size of the upstream boundary layer effect, the drag coefficient was measured on an isolated spire with $\frac{b}{h} = 0.15$ at four values of h. The results, corrected for blockage using $\theta = 1.7$, are plotted against 1/h in Figure 13, the intercept at $1/h = 0$ being interpreted as giving C_{D_∞} for zero floor boundary layer thickness. For the range of h tested the floor boundary layer effect can be seen to be small, not exceeding 3% even for the smallest spires which had $h = 0.305$ m.

4.4 Effects of b/h and the Splitter Plate

Figure 14 shows a plot of C_{D_∞}, the drag coefficient of an isolated spire, versus b/h. The data were obtained on a set of spires with $h = 0.914$ m at various b/h and were corrected for blockage using $\theta = 1.7$ and for the floor boundary layer effect using Figure 13. Thus it was effectively assumed that the value for θ of 1.7 and the results in Figure 13 applied not only to $b/h = 0.15$ but to all other values of b/h in the range $0.05 < b/h < 0.30$. In Figure 8 it can be seen that C_{D_∞} decreased from a value of 1.47 at $\frac{b}{h} = 0.05$ to 1.30 at $b/h = 0.3$.

At the end of the drag measurements the splitter plate was removed from the spire with dimensions $h = 0.914$ m and $b/h = 0.15$ and C_{D_∞} was remeasured. The single point in Figure 14 for the case without the splitter plate can be seen to be very close to the curve through the rest of the data showing the splitter plate had only a small effect on the spire drag.

4.5 C_{D_O} for an Array of Spires Spaced at Intervals of $\frac{1}{2}h$

Since a spacing of $\delta y = \frac{1}{2}h$ has proven to give good lateral uniformity of the flow at 6h downstream(2) and is often used in practice, it is desirable to know the value of C_{D_O}, which includes interference effects, at this spacing for various values of b/h. The interference factor, F_I, by which C_{D_∞} must be multiplied to obtain C_{D_O}, can be expected to depend on $\frac{b}{\delta y}$ and $\frac{h}{\delta y}$. However, it seems reasonable to assume that F_I is much more sensitive to $\frac{b}{\delta y}$ than to $\frac{h}{\delta y}$. If the dependence on $\frac{h}{\delta y}$ is neglected completely then F_I depends only on $\frac{b}{\delta y}$ and Figure 12(b), which was obtained by varying δy while h stayed constant, becomes generally valid. This assumption will be adopted here. For the case where $\delta y = \frac{1}{2}h$ the value of F_I was therefore obtained for various values of $\frac{b}{h}$ from Figure 12(b) by reading off the curve at $\frac{b}{\delta y} = 2\frac{b}{h}$. The following table gives the values so obtained and the resulting C_{D_O} for a range of b/h.

b/h	F_I	C_{D_∞}(From Fig. 14)	$C_{D_O} = F_I C_{D_\infty}$
.06	1.000	1.455	1.45
.08	1.016	1.425	1.45
.10	1.040	1.400	1.46
.15	1.082	1.360	1.47
.20	1.062	1.330	1.41
.25	0.990	1.315	1.30

From the table it can be seen that the combined effects of $\frac{b}{h}$ and interference, lead to an almost constant value of C_{D_O} in the range $0.06 < b/h < 0.20$ for $\frac{1}{2}$h spacing, the value being close to 1.45. A further experimental investigation of the interference effect would be useful in which $\frac{b}{h}$ were varied while maintaining $\frac{h}{\delta y}$ constant at 2, thus obviating the need for the present assumption that interference was independent of $h/\delta y$.

The value 1.45 for C_{D_O} is below the value 2.0 assumed by Campbell and Standen$^{(2)}$. However, for their calculation procedure to give better results a higher rather than a lower C_{D_O} is required so it is not improved by the new value.

4.6 Velocity Measurements and Flow Visualization

The velocity and flow visualization experiments were carried out on an array of three spires at $\frac{1}{2}h$ spacing with dimension $h = 1.219$ m and $\frac{b}{h} = 0.15$. Vertical profiles of the longitudinal mean velocity and turbulence intensity were measured at three positions: (a) midway between two spires at the spire station, (b) one spire height downstream of position (a), and (c) one spire height downstream of the middle spire centre-line. The results are shown in Figures 15(a), (b) and (c). The mean velocity profile at position (a) has been normalized by the average velocity, $\overline{U}$, at that traverse position rather than U_e in order to facilitate comparison with the form of velocity profile implied by the theoretical assumptions of Reference 2, which is

$$U = U_e \quad \text{for } z \geq h$$

$$U = U_e\left(\frac{z}{h}\right)^{\alpha}\left(1 - 2\frac{b}{h}(1 - z/h)\right)^{-1} \quad \text{for } z \leq h \qquad (39)$$

The value of α was taken to be 0.25 in computing the curve in Figure 15(a). The main difference between Equation 39 and the measured profile is near to the floor where Equation 39 gives too low a velocity which would result in the theory of Reference 2 making the spires too wide in this region.

At one spire height downstream, Figures 15(b) and (c), the wakes from the spires had already coalesced in the region below $\frac{z}{h} = 0.5$. The mean velocity profile downstream of the spire centre-line (Fig. 15(c)) exhibited a definite kink near the floor that was attributed to large vortices, with axes parallel to the flow direction, originating from the spire base. The turbulence intensity near the floor at one spire height downstream was approximately 20% of the free stream velocity.

Figures 16 and 17 show photographs of the smoke patterns observed. The flow was inclined upwards just upstream of the spire station and then turned downwards again downstream of a spire centreline. Between spire centrelines the downstream flow was roughly horizontal near $z = h$ but was inclined slightly upwards at low values of $\frac{z}{h}$. Strong evidence of vortices aligned with their axes parallel to the flow is evident in some of the photographs.

5. A SUMMARY OF PAST WIND SIMULATIONS

Since Reference 3 was written the spire-roughness technique has been used by the Laboratory to simulate a wide range of planetary boundary layers. The data on the boundary layer simulations tend to be scattered amongst the reports on the individual projects for which they were generated making it difficult to form an overall assessment. Therefore, in Figures 18 to 25 a summary is given of six simulations with exponents ranging from 0.53 down to 0.10. Most of the spires had flared bases but there is little to indicate, either in the Figures or in other less documented cases, that the flared base performed any useful role other than, as in Figure 20, providing a convenient method for making small changes to the total spire area. The triangular spires of Figure 21 and the nearly triangular spires of Figure 23 did not perform noticeably worse than the others, and exponents higher than 0.4 have been successfully generated using triangular spires (unpublished). Figure 23 shows that even with very thin spires the flow is effectively uniform at $x_o \doteq 6h$.

Harris$^{(14)}$ reviewed wind properties and concluded that in the neutral planetary boundary layer the turbulence intensity, $\frac{u'}{U_e}$, near the ground varies only slightly with α. He gives the values $\frac{u'}{U_e} = 0.106$ at $\alpha = 0.16$ and $\frac{u'}{U_e} = 0.115$ at $\alpha = 0.40$. The data in Figures 18 to 21 agree well with this range and the data for $\alpha = 0.16$ in Figure 22 would also if the decrease in $\frac{u'}{U_e}$ near the floor, which was due to insufficient floor roughness, were ignored. Figure 23 is for a very smooth exposure, such as over open water, so a lower value of $\frac{u'}{U_e}$ near the floor is to be expected. Figure 24 shows the turbulence intensity data from all six simulations expressed at full scale on one plot and the intensities are based on local mean wind speed in order to facilitate comparison with full scale data. Three sets of full scale measurements $^{(14,15,16)}$ are included and the agreement can be seen to be remarkably good. Again, insufficient floor roughness is the reason why the $\alpha = 0.16$ data behaved differently at low values of z from the rest of the data. De Croos and Gartshore$^{(17)}$ have published results from a single spire generated boundary layer that disagree with the present body of data on turbulence intensity and with the full scale data. A possible explanation for this discrepancy (Gartshore, personal communication) was the presence of a strut on the downstream side of their spires that presented a large area to the flow.

The case in Figure 22, which was for a full aeroelastic model of Lions' Gate Bridge, is the one for which the most extensive measurements were made, including the intensity of the vertical turbulence component and the lateral cross-correlations. Other measured quantities not included here, but given in References 11, 18 and 19, were the shear correlation coefficient and cross-spectra of velocities for various lateral separations. Full scale wind measurements have been made on the bridge(20), and are still underway. So far insufficient data at high wind speeds have been obtained to make a worthwhile comparison with the wind tunnel simulation. Considering the ratio $\frac{w'}{u'}$, the results in Figure 22 indicate it was slightly high as compared with the consensus of full scale data near the ground which give the ratio as approximately 0.5. The ratio might have been improved if more floor roughness had been present. The lateral correlations, $\frac{\overline{u(o)u(y)}}{u'^2}$ and $\frac{\overline{w(o)w(y)}}{w'^2}$, gave integral scales of 0.21 and 0.20 m respectively when integrated to the point where the correlation first reached zero. These become 23 and 22 m when expressed at full scale. There are, as yet, very few full scale measurements of lateral correlations close to the height concerned (approximately 67 m) so it is difficult to assess the model values. Shiotani and Arai(21) presented full scale correlation measurements of longitudinal turbulence at high wind speeds at $z = 40$ m. However, the wind was not normal to the line of anemometers so their integral scales, which lay in the range 40 to 80 m, are not true lateral scales and probably overestimate L_u^y. Unpublished data at lower speeds, with the wind 40 degress off normal to the line of anemometers, have been obtained from the Lions' Gate Bridge anemometers and yielded a value close to 50 m for both the longitudinal and vertical turbulence. This is again probably an overestimate.

Grant$^{(22)}$ measured lateral correlations in a naturally grown laboratory boundary layer on a smooth surface. Using interpolation and integrating his data to the point where the correlations first reached zero, they indicate that at $z = 0.3\delta$ (the height of the correlation data in Figure 22) $L_u^y \simeq 0.15\delta$ and $L_w^y \simeq 0.10\delta$. The comparable values of Figure 22 are $L_u^y \simeq L_w^y \simeq 0.10\delta$.

It is nearly always found that the overall form of the power spectrum of artificially generated turbulence is similar to that at full scale under neutral conditions. However, the position of the power spectrum curve along the frequency axis is sensitive to the way in which the turbulence is generated, whether by spires or by a grid for example. The longitudinal integral scale, L_u^x, is closely connected with the position of the power spectrum curve. Figure 25 compares L_u^x, obtained by fitting von Karman's spectrum to the data from various spire-roughness boundary layers, with Teunissen's survey$^{(23)}$ of full scale data. The spire-roughness data are scattered but lie almost entirely within the range of the full-scale data.

It is unlikely that at $\frac{x_o}{h} = 6$ the boundary layer has approached an equilibrium state and evidence that it is still developing has been given by De Croos and Gartshore(17). However, the differences are not large and appear unlikely to be of any importance in practice. In fact, it is questionable whether the state of equilibrium should be the ultimate aim in boundary layer simulation since the planetary boundary layer itself is continually adjusting to changes in surface roughness.

6. CONCLUSIONS

(i) There is little evidence to suggest that the spire shape need be more complex than a triangle.

(ii) The drag coefficient of triangular spires is 1.45 for half-height spacing and $0.06 < \frac{b}{h} < 0.20$. The presence of a splitter plate has little effect on the drag.

(iii) For triangular spires Equation 18 (or Figure 5) gives the required based to height ratio, assuming the floor roughness has been appropriately chosen using, for example, Reference 6. The suggested value for the blockage factor, θ, is 1.0 for spires mounted at the exit plane of the contraction.

(iv) Since 1972, the spire roughness technique has been extended to cover the full range of boundary layers with exponents from 0.1 to 0.5. The mean velocity profile, longitudinal turbulence intensity and integral scale L_u^x compare well with neutral planetary boundary layer data and, as far as can be assessed, other turbulence properties are also of the right order.

REFERENCES

1. Templin, R.J. "Interim Progress Note on Simulation of Earth's Surface Winds by Artificially Thickened Wind Tunnel Boundary Layers", National Research Council of Canada, NAE. Report LTR-LA-22, Feb. 1969.

2. Campbell, G.S. and Standen, N.M. "Progress Report II on Simulation of Earth's Surface Winds by Artificially Thickened Wind Tunnel Boundary Layers", National Research Council of Canada, NAE. Report LTR-LA-37, July 1969.

3. Standen, N.M. "A Spire Array for Generating Thick Turbulent Shear Layers for Natural Wind Simulation in Wind Tunnels", National Research Council of Canada, NAE. Report LTR-LA-94, May 1972.

4. Cowdrey, C.F. "A Simple Method for the Design of Wind-Tunnel Velocity-Profile Grids", National Physical Laboratory Aero. Note 1055, May 1967.

5. Maskell, E.C. "A Theory of the Blockage Effects on Bluff Bodies and Stalled Wings in a Closed Wind Tunnel", ARC. R&M 3400, 1963.

6. Wooding, R.S., Bradley, E.F., and Marshall, J.K. "Drag due to Regular Arrays of Roughness of Varying Geometry," Boundary Layer Meteorology, Vol. 5, 1973, pp. 285 - 308.

7. Gartshore, I.S. "A Relationship Between Roughness Geometry and Velocity Profile Shape for Turbulent Boundary Layers", National Research Council of Canada, NAE Report LTR-LA-140, Oct. 1973.

8. Cowdrey, C.F. "Two Topics of Interest in Experimental Industrial Aerodynamics,", Symposium on Wind Effects on Buildings and Structures, Loughborough University, April 1968, Paper 29.

9. Irwin, H.P.A.H. and Wardlaw, R.L. "A Wind Tunnel Investigation of a Retractable Fabric Roof for the Montreal Olympic Stadium", Proceedings of the Fifth International Conference on Wind Engineering, Colorado State University, July 1979. (NAE Report LTR-LA-228, 1979).

10. Dalgliesh, W.A., Templin, J.T. and Cooper, K.R. "Comparisons of Wind Tunnel and Full-Scale Building Surface Pressures with Emphasis on Peaks", Proceedings of the Fifth International Conference on Wind Engineering Colorado State University, July 1979.

11. Irwin, H.P.A.H and Schuyler, G.D. "Experiments on a Full Aeroelastic Model of Lions' Gate Bridge in Smooth and Turbulent Flow", National Research Council of Canada, NAE Report LTR-LA-206, June 1977.

12. Irwin, H.P.A.H. "Further Investigations of a Full Aeroelastic Model of Lions' Gate Bridge". National Research Council of Canada, NAE Report LTR-LA-221, May 1978.

13. Gould, R.W.F. 'Wake Blockage Corrections in a Closed Wind Tunnel for One or Two Wall-Mounted Models Subject to Separated Flow", A.R.C. R & M No. 3649, Feb. 1969.

14. Harris, R.I. "The Nature of the Wind", Proceedings of the Seminar on the Modern Design of Wind Sensitive Structures, Institute of Civil Engineers, London, pp.29 - 55, 1971.

15. Duchène-Marullaz, P. "Full-Scale Measurements of Atmospheric Turbulence in a Suburban Area", Proceedings of the Fourth International Conference on Wind Effects on Buildings and Structures, Heathrow, 1975, pp.23 - 21

16. Jackson, P. 'Wind Structure Near a City Centre", Boundary Layer Meteorology, Vol. 15, 1978, pp.323 - 340.

17. De Croos, K.A., and Gartshore, I.S. "A Comparison of Atmospheric Wind Simulations" Proceedings of the Third U.S. National Conference on Wind Engineering, Feb. 1978, pp. 497 - 500.

18. Irwin, H.P.A.H. "Wind Tunnel and Analytical Investigations of the Response of Lions' Gate Bridge to a Turbulent Wind", National Research Council of Canada, NAE Report LTR-LA-210, June 1977.

19. Irwin, H.P.A.H. "Cross-Spectra of Turbulence Velocities in Isotropic Turbulence", Boundary Layer Meteorology, Vol. 16, 1979.

20.	Williams, C.D., Teunissen, H.W. and Irwin, H.P.A.H.	"The Lions' Gate Bridge - Wind Measurements and Wind Tunnel Investigations", The Second Canadian Workshop on Wind Engineering, Varennes, Quebec, Sept. 1978, (Proceedings in press).
21.	Shiotani, M., and Arai, H.	"Lateral Structures of Gusts in High Winds", Proceedings of the Second International Conference on Wind Effects on Buildings and Structures, Ottawa, Sept. 1967, pp535 - 555.
22.	Grant, H.L.	"The Large Eddies of Turbulent Motion", J. Fluid Mechanics, Vol. 4, pp. 149 - 190, 1958.
23.	Teunissen, H.W.	"Characteristics of the Mean Wind and Turbulence in the Planetary Boundary Layer", University of Toronto, Institute for Aerospace Studies, UTIAS Review 32, Oct. 1970.

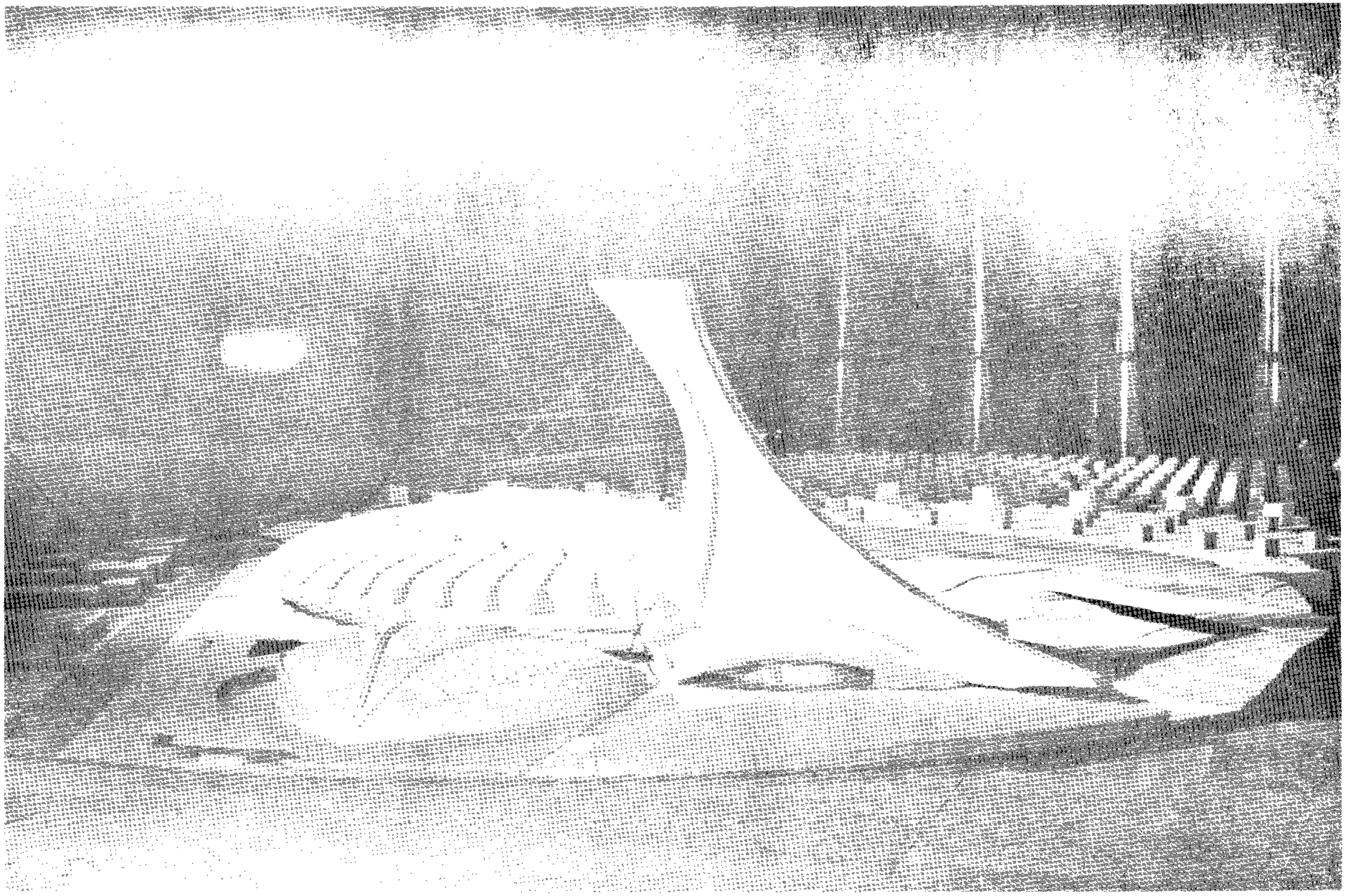

FIG I APPLICATION OF THE SPIRE ROUGHNESS TECHNIQUE FOR A 1:100 SCALE WIND TUNNEL INVESTIGATION OF THE MONTREAL OLYMPIC STADIUM (9)

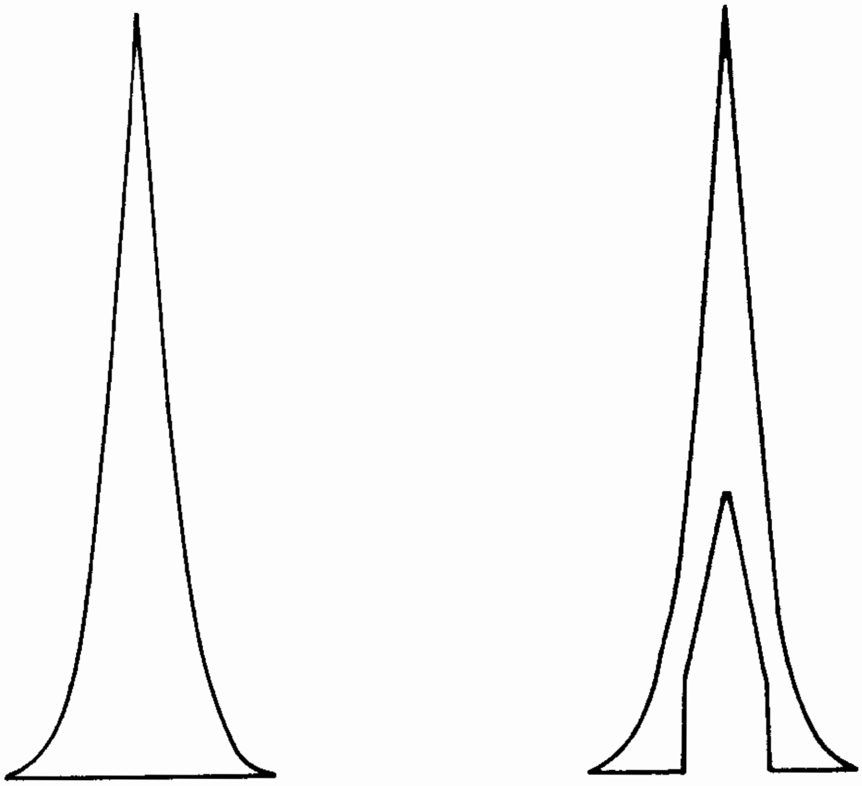

As originally designed

Modified version

FIG 2 EXAMPLE OF AN AD-HOC MODIFICATION (3)

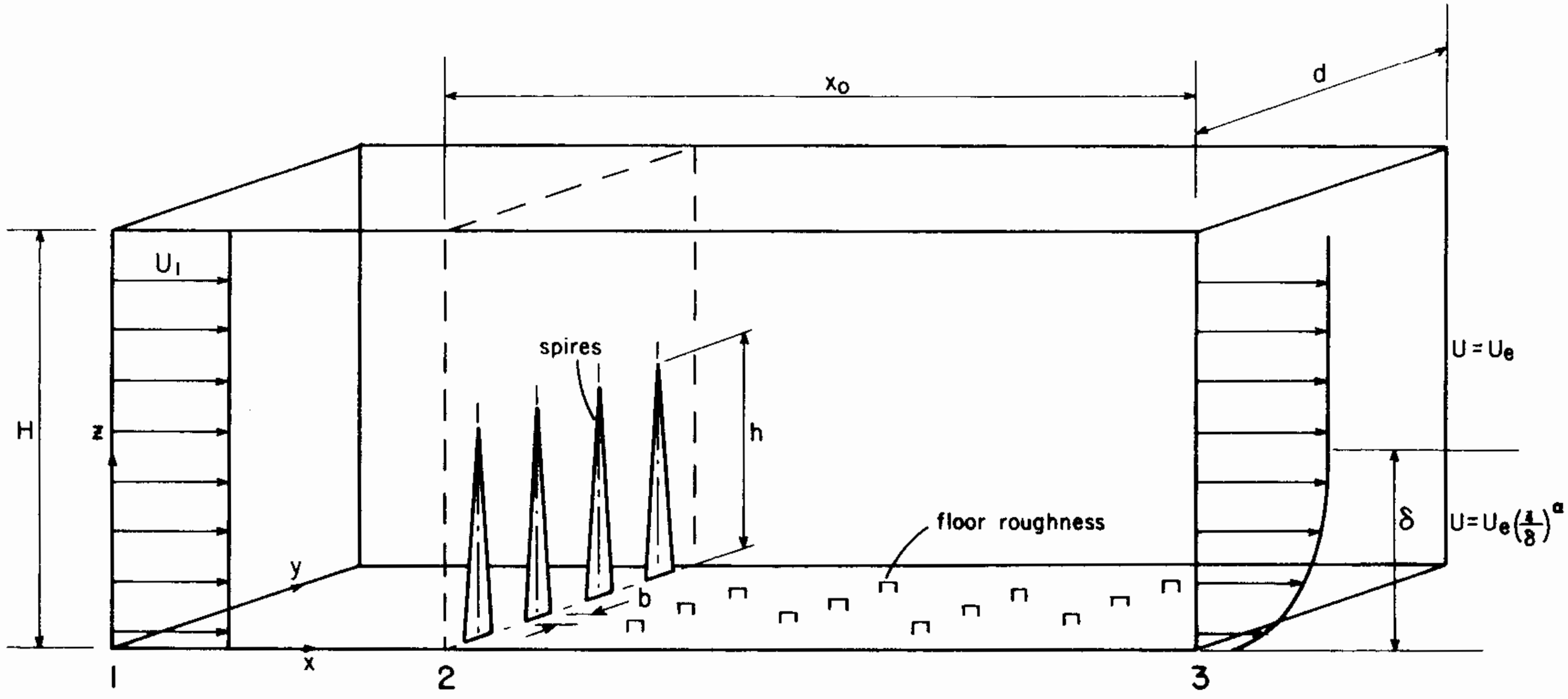

FIG 3 RECTANGULAR WORKING SECTION AS A CONTROL VOLUME

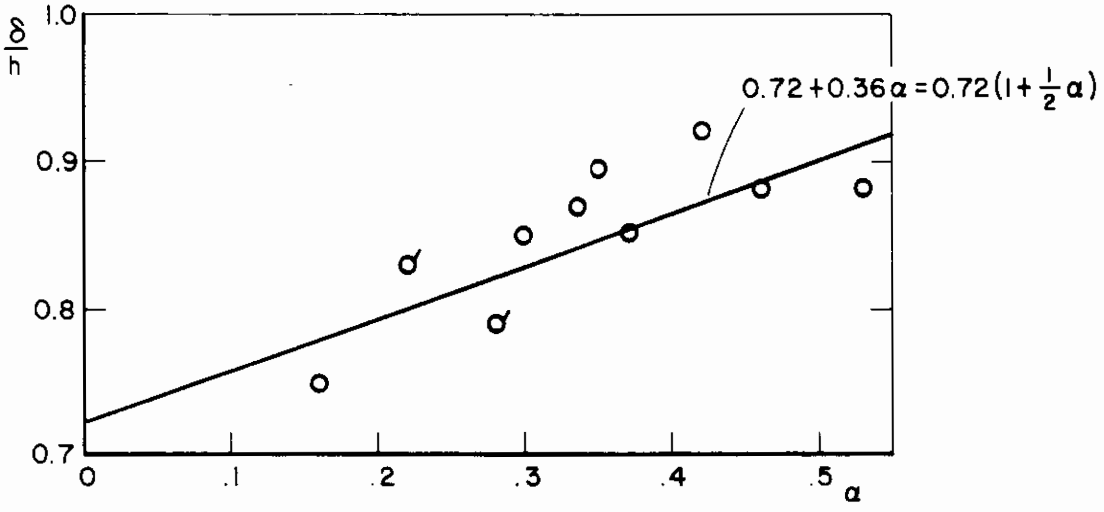

FIG 4 DEPENDENCE OF δ/h ON α AT $x_0=6h$

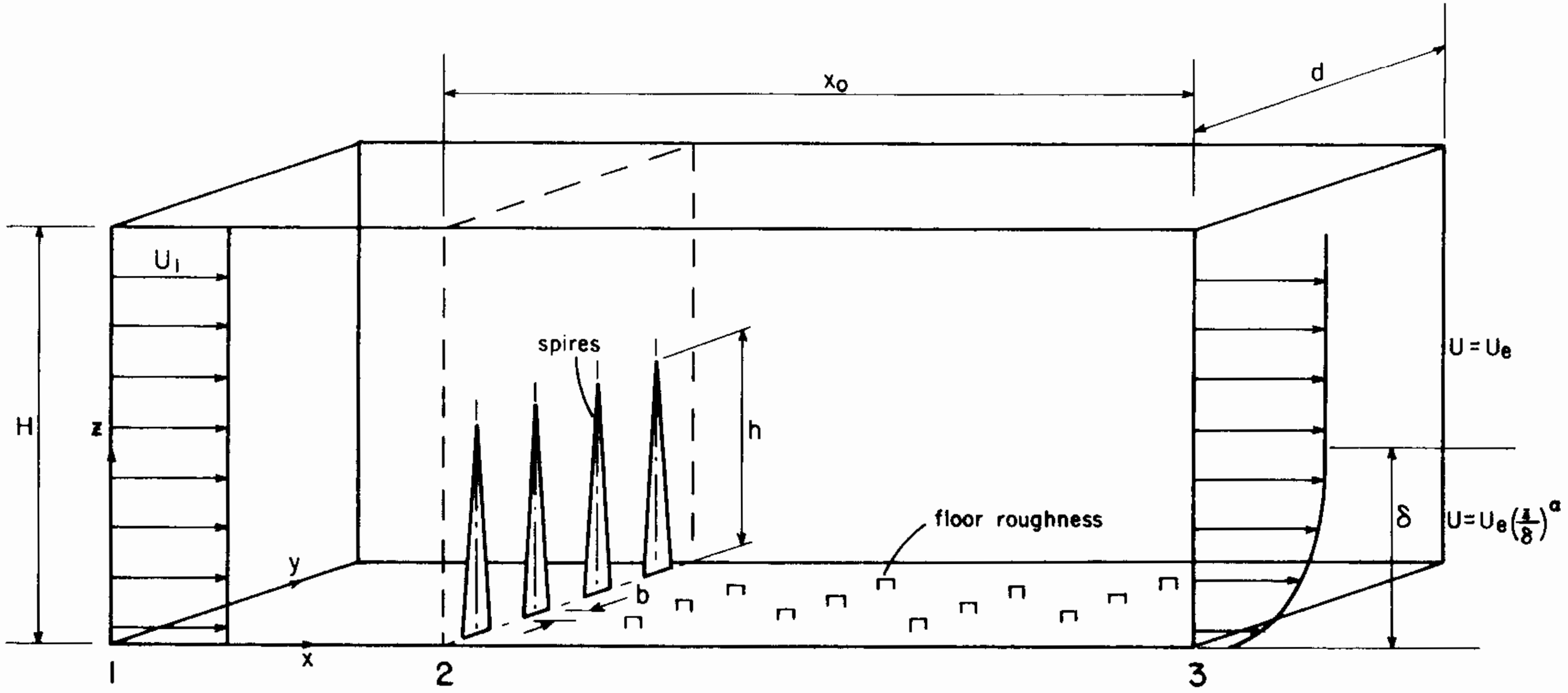

FIG 3 RECTANGULAR WORKING SECTION AS A CONTROL VOLUME

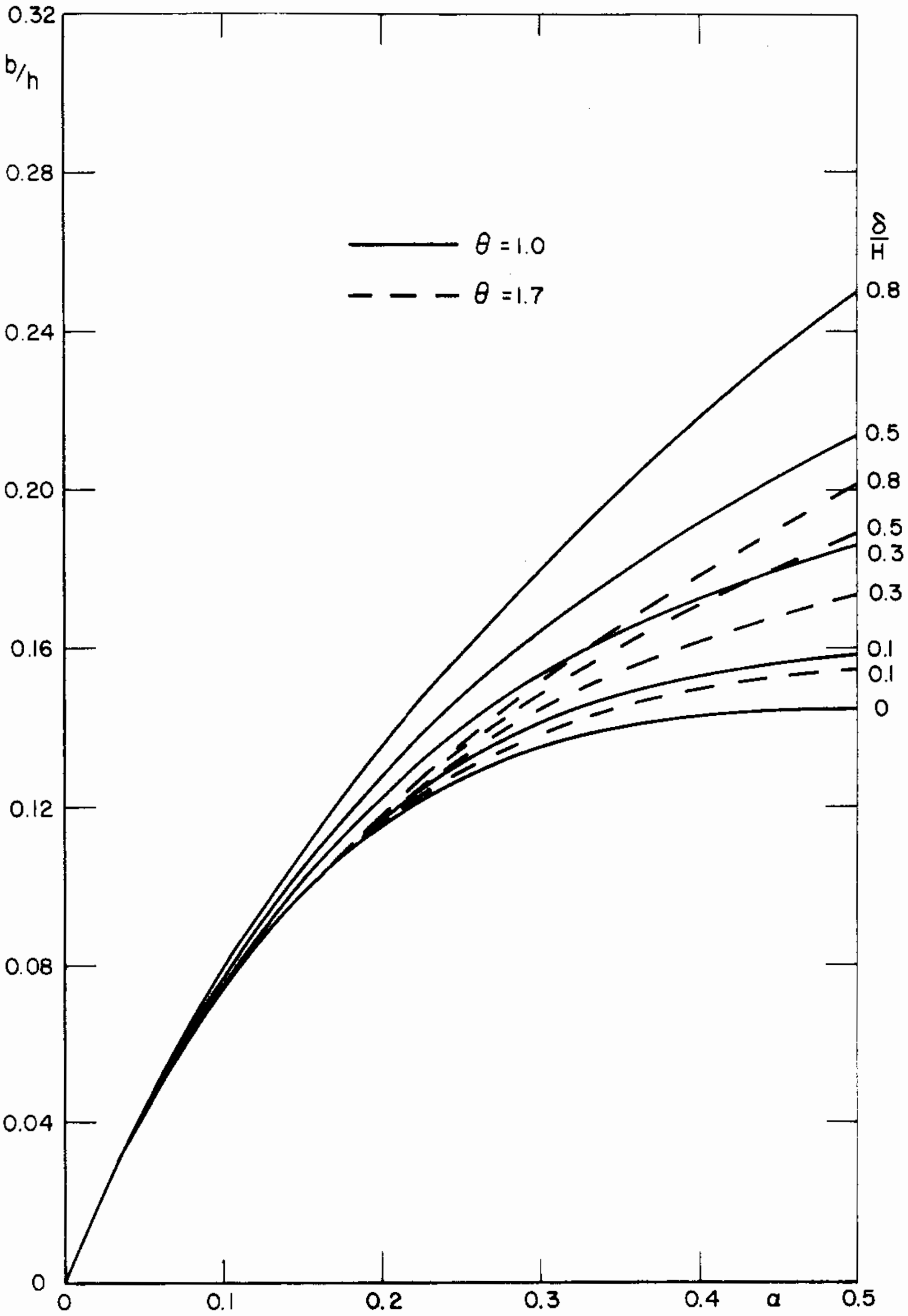

FIG 5 BASE TO HEIGHT RATIO FOR TRIANGULAR SPIRES ACCORDING TO EQUATION 18

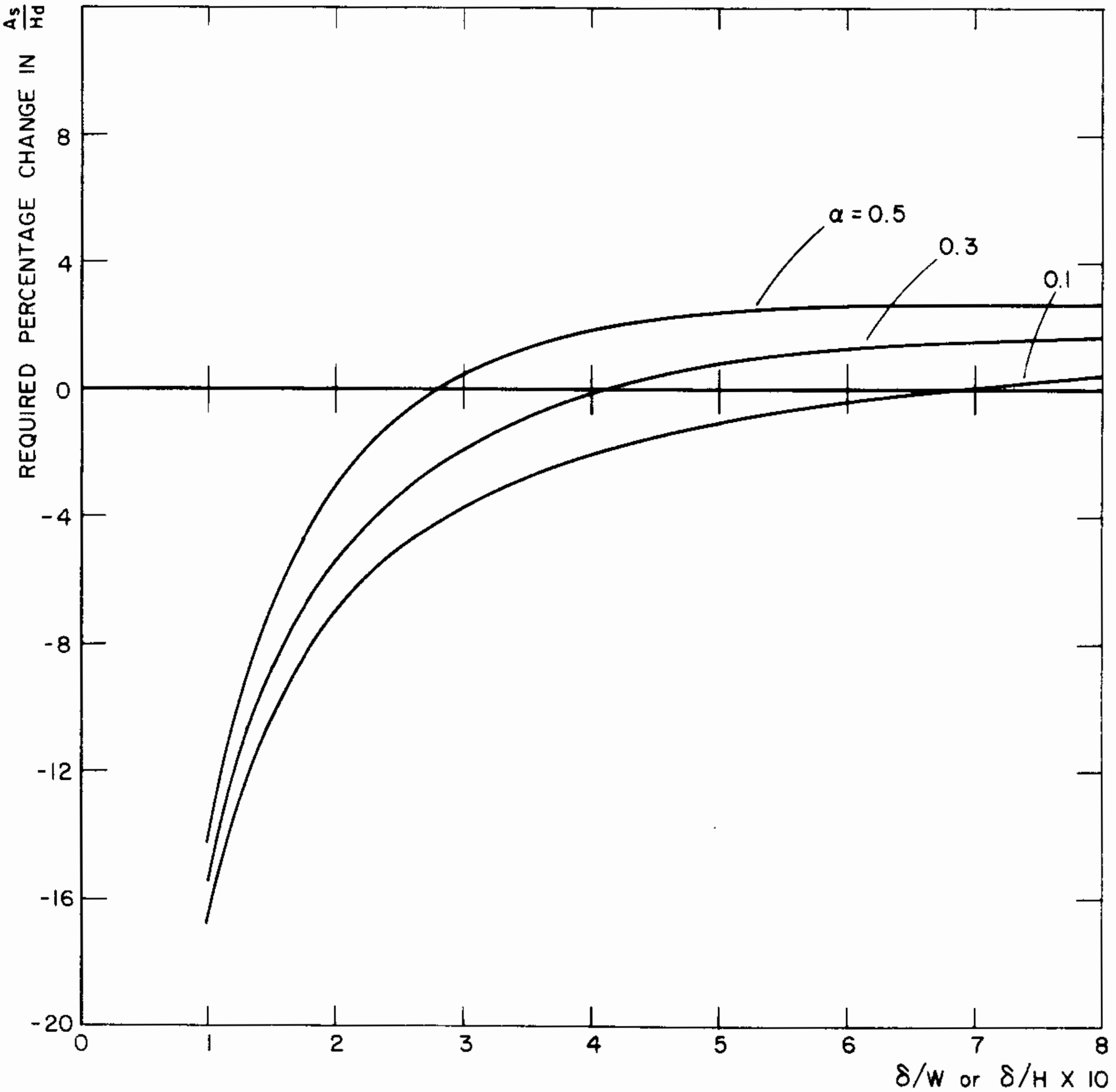

FIG 6 EFFECT OF CORNER FILLETS IN A SQUARE WORKING SECTION. W=0.1 H

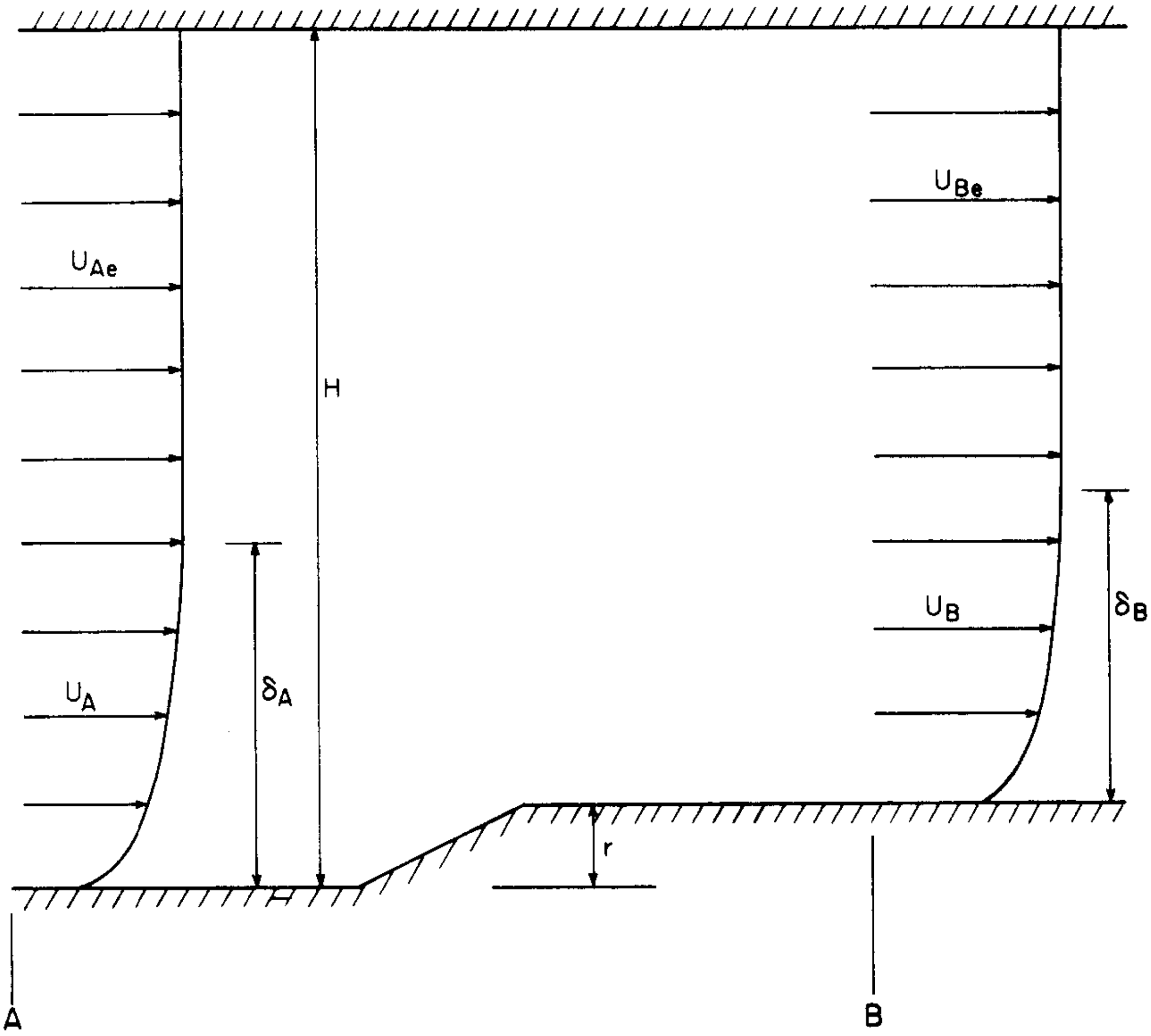

FIG 7 RAMP DOWNSTREAM OF SPIRES

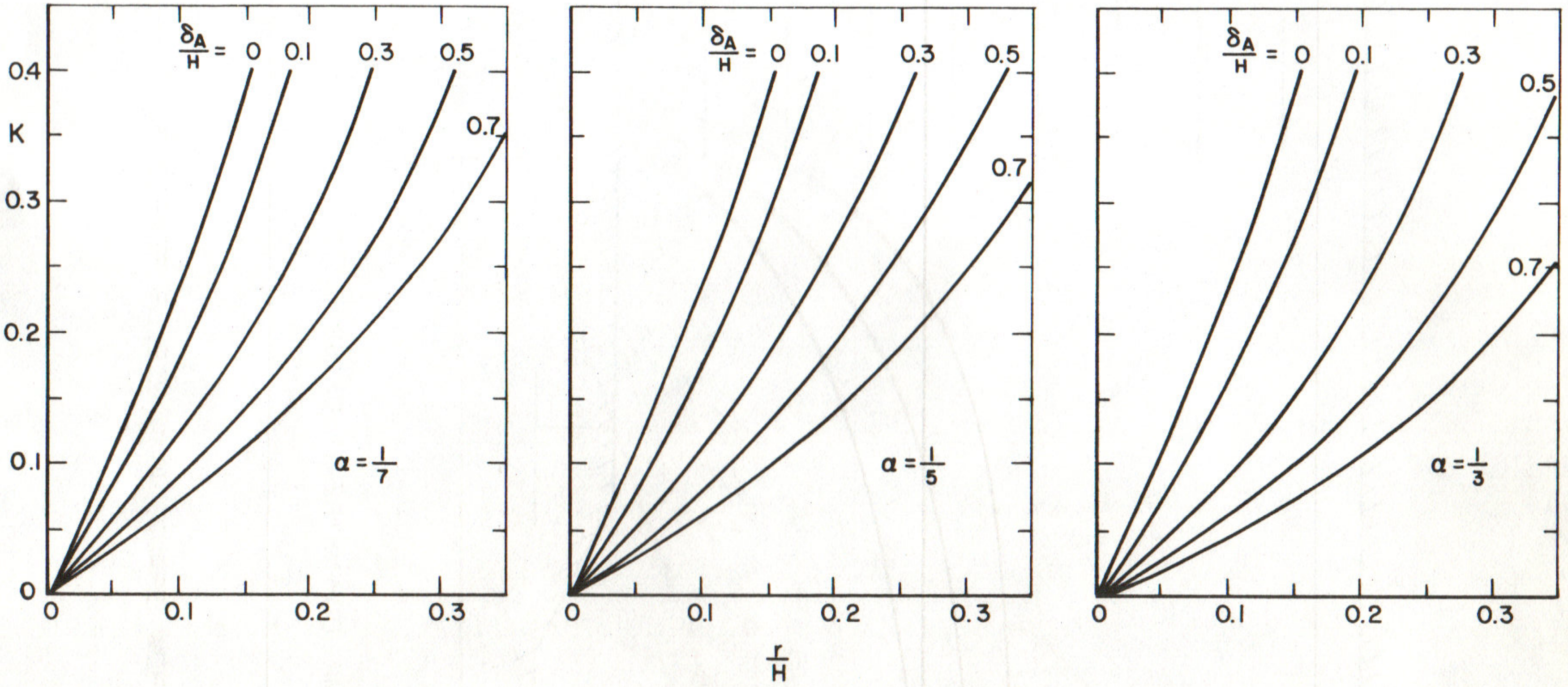

FIG 8 CALCULATED PRESSURE DROP COEFFICIENT, K, OVER A RAMP WITH VARIOUS FLOOR BOUNDARY LAYERS IN THE APPROACH FLOW

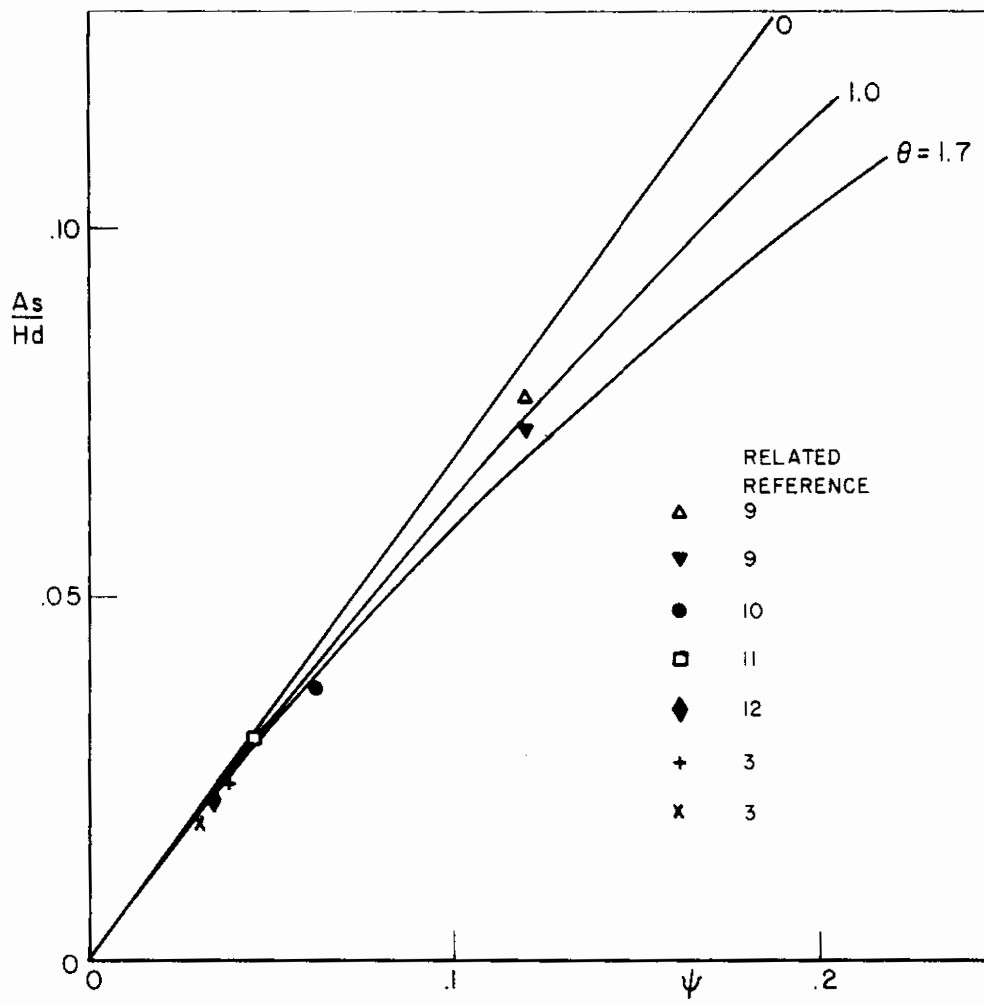

FIG 10 COMPARISON OF THEORY WITH PAST WIND SIMULATION DATA

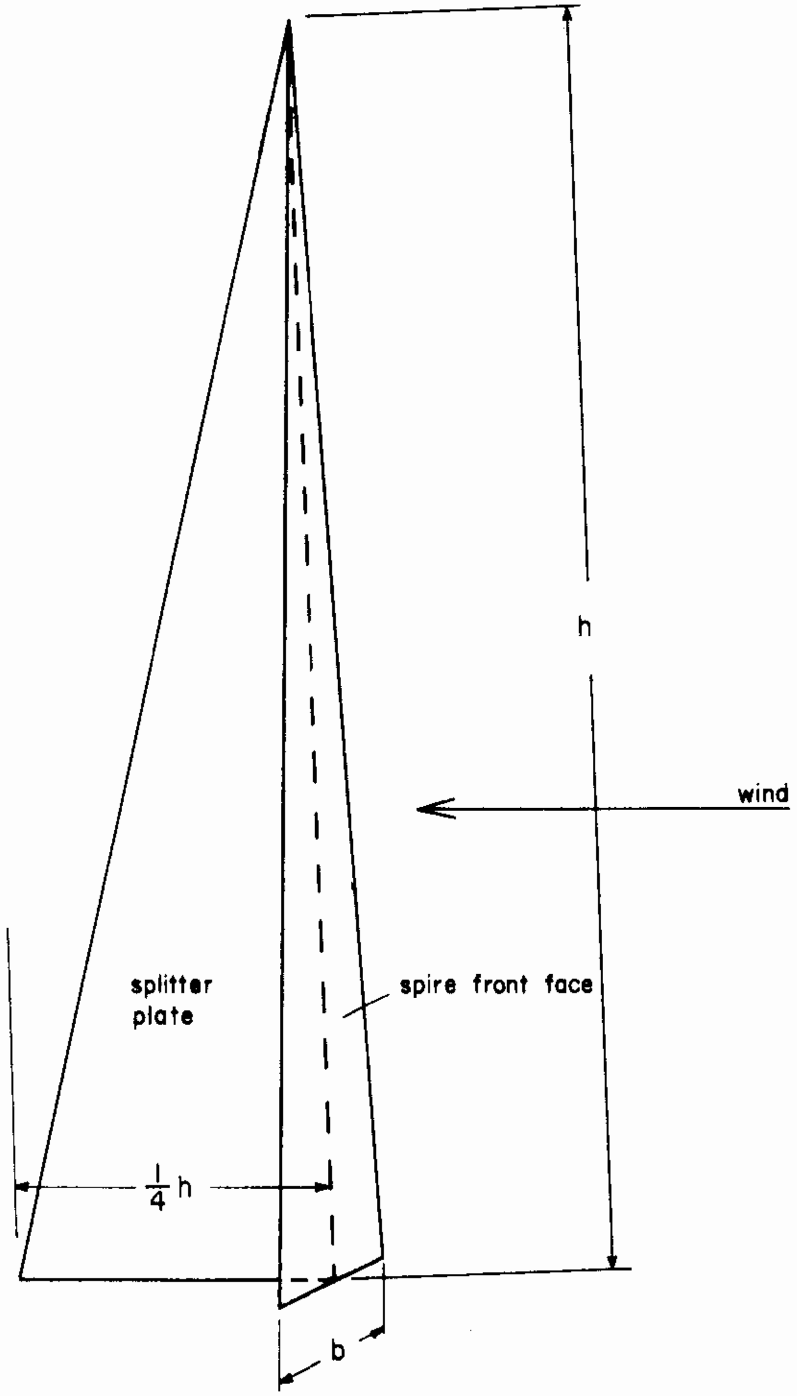

FIG II TRIANGULAR SPIRE WITH SPLITTER PLATE

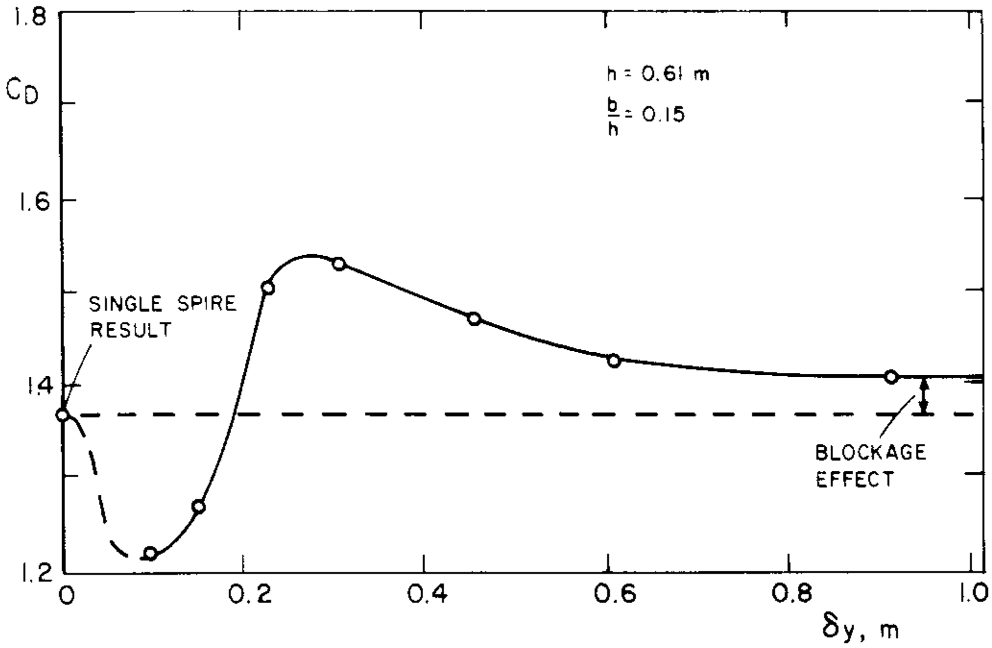

FIG 12(a) EFFECT OF ADJACENT SPIRES ON DRAG COEFFICIENT

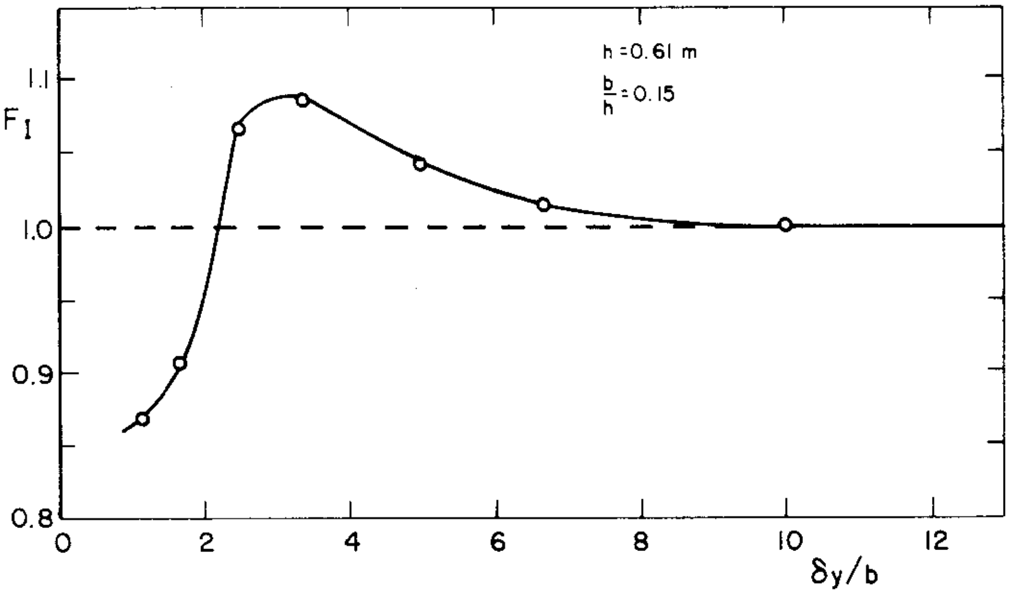

FIG 12(b) INTERFERENCE FACTOR

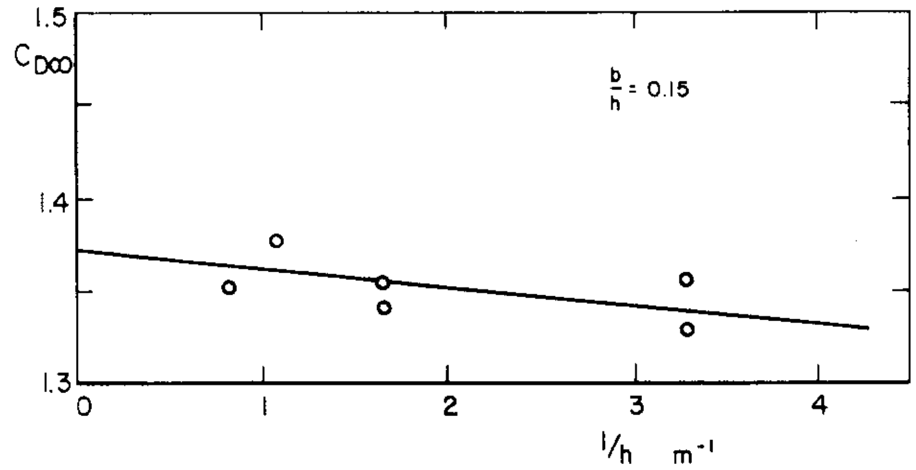

FIG. 13 EFFECT OF UPSTREAM FLOOR BOUNDARY LAYER ON THE DRAG COEFFICIENT OF AN ISOLATED SPIRE

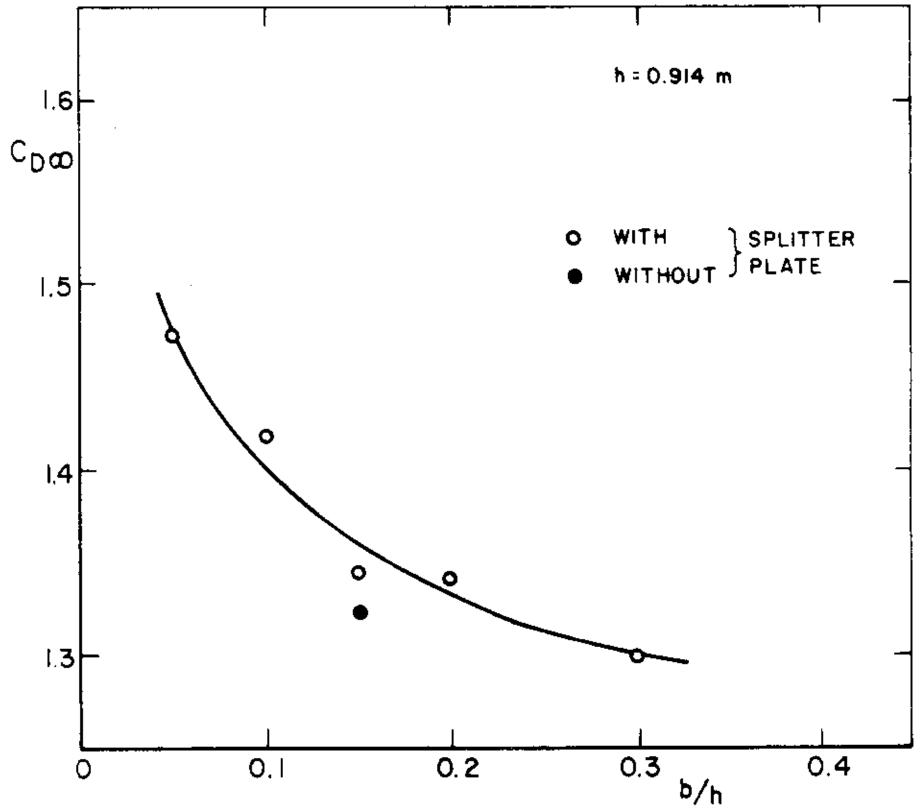

FIG 14 EFFECT OF b/h ON THE DRAG COEFFICIENT OF AN ISOLATED SPIRE

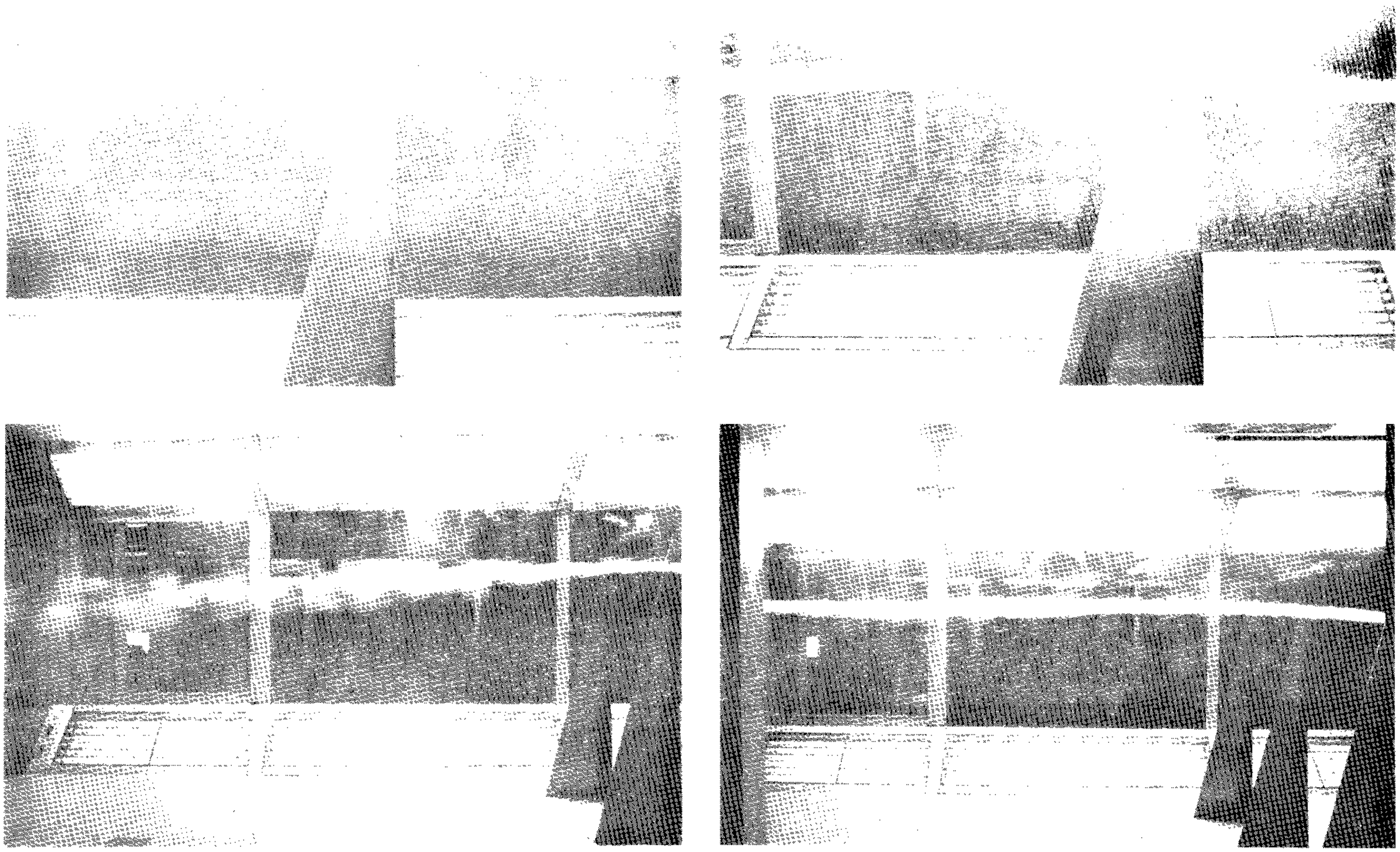

ON SPIRE CENTRE-LINE

BETWEEN SPIRE CENTRE-LINES

FIG 16 FLOW VISUALIZATION NEAR THE TOP OF THE SPIRES

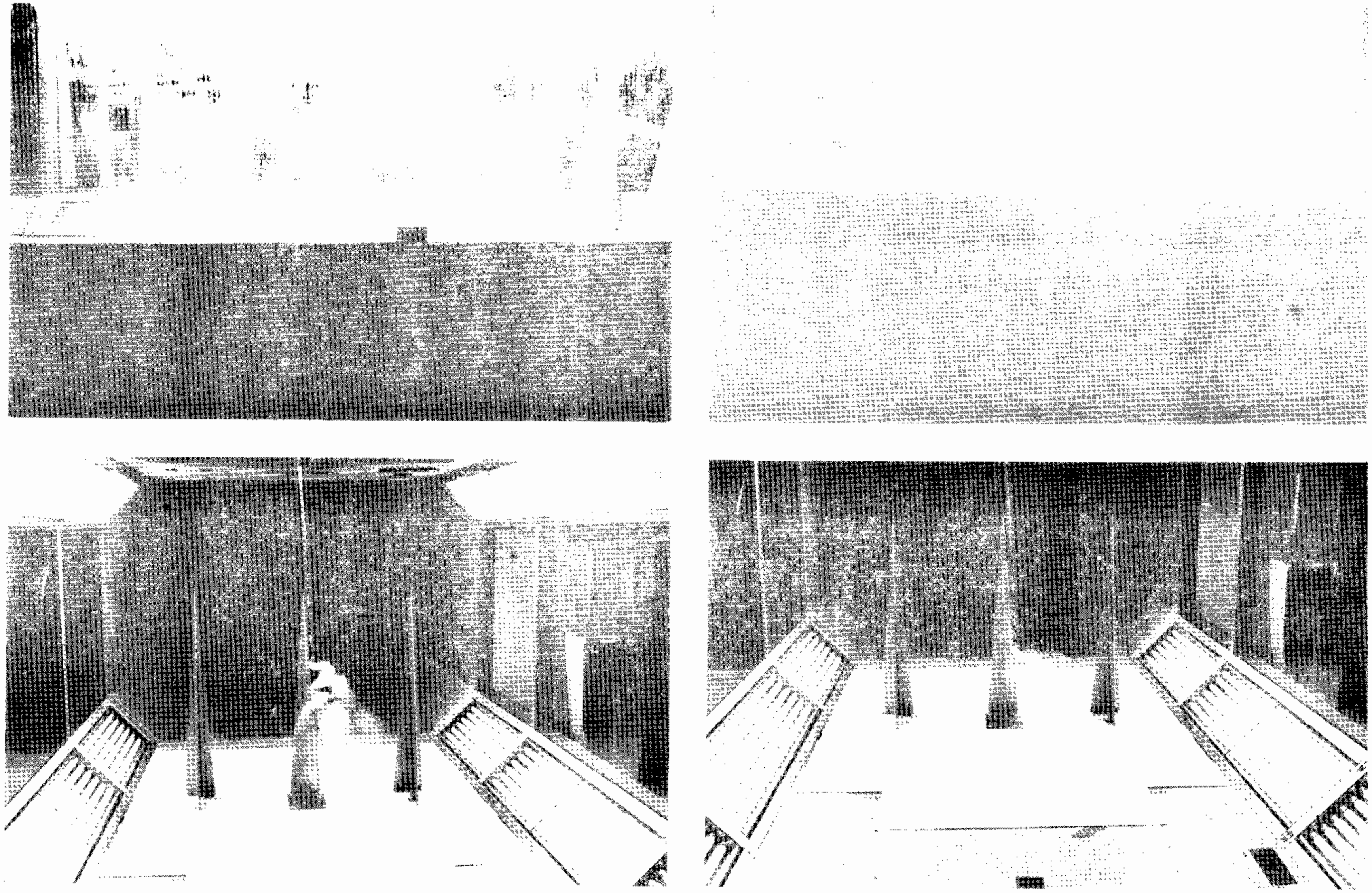

FLOW AT HALF HEIGHT

FLOW NEAR THE BASE

FIG 17 FLOW VISUALIZATION SHOWING AXIALLY ALIGNED VORTICES

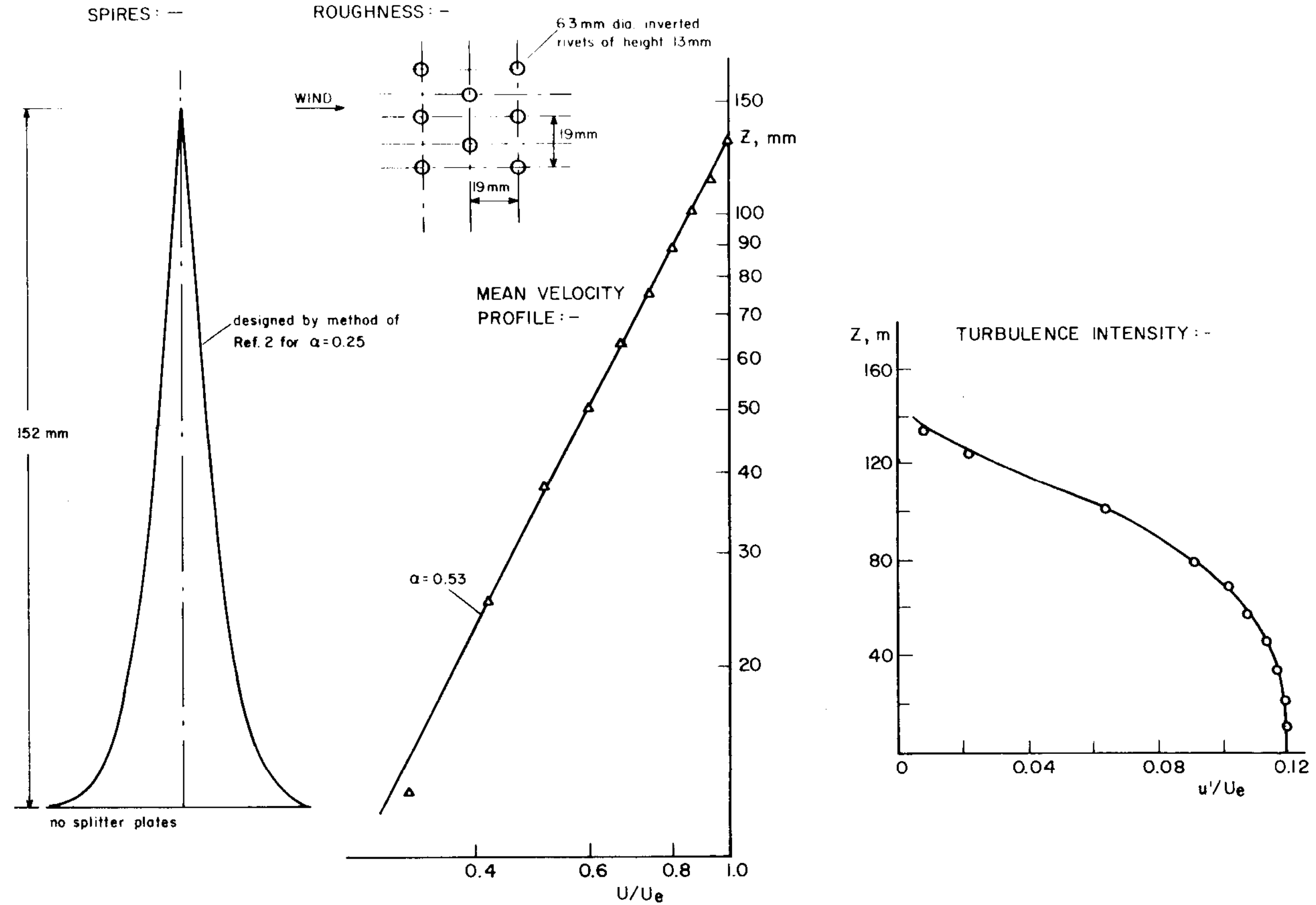

FIG 18 1:3500 SCALE VERY ROUGH TERRAIN SIMULATION. $x_o = 6h$

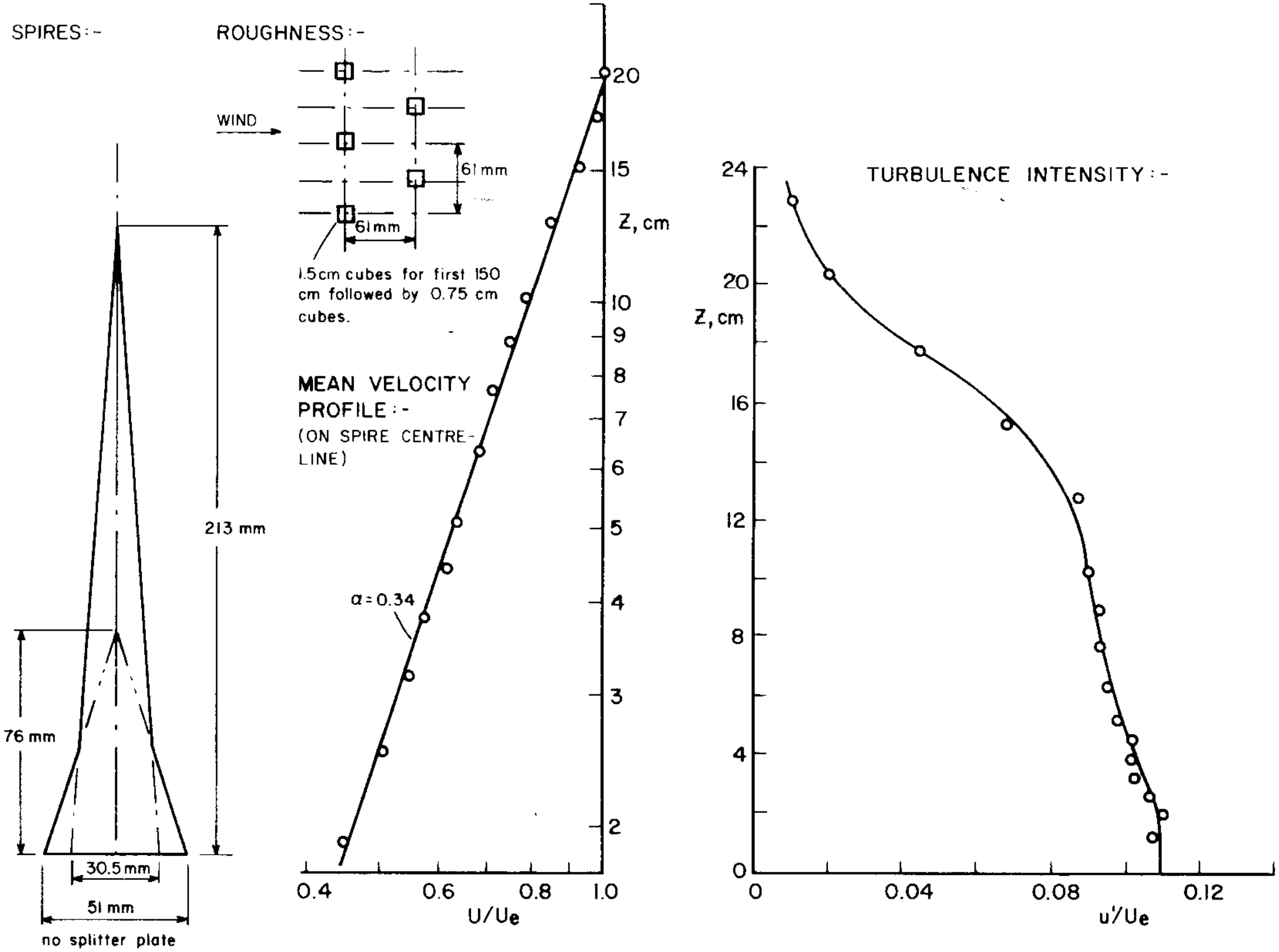

FIG 19 1:2000 SCALE SUBURBAN BOUNDARY LAYER SIMULATION (UNPUBLISHED WORK IN CONNECTION WITH REF 10) DATA AT $x_0 = 10H$

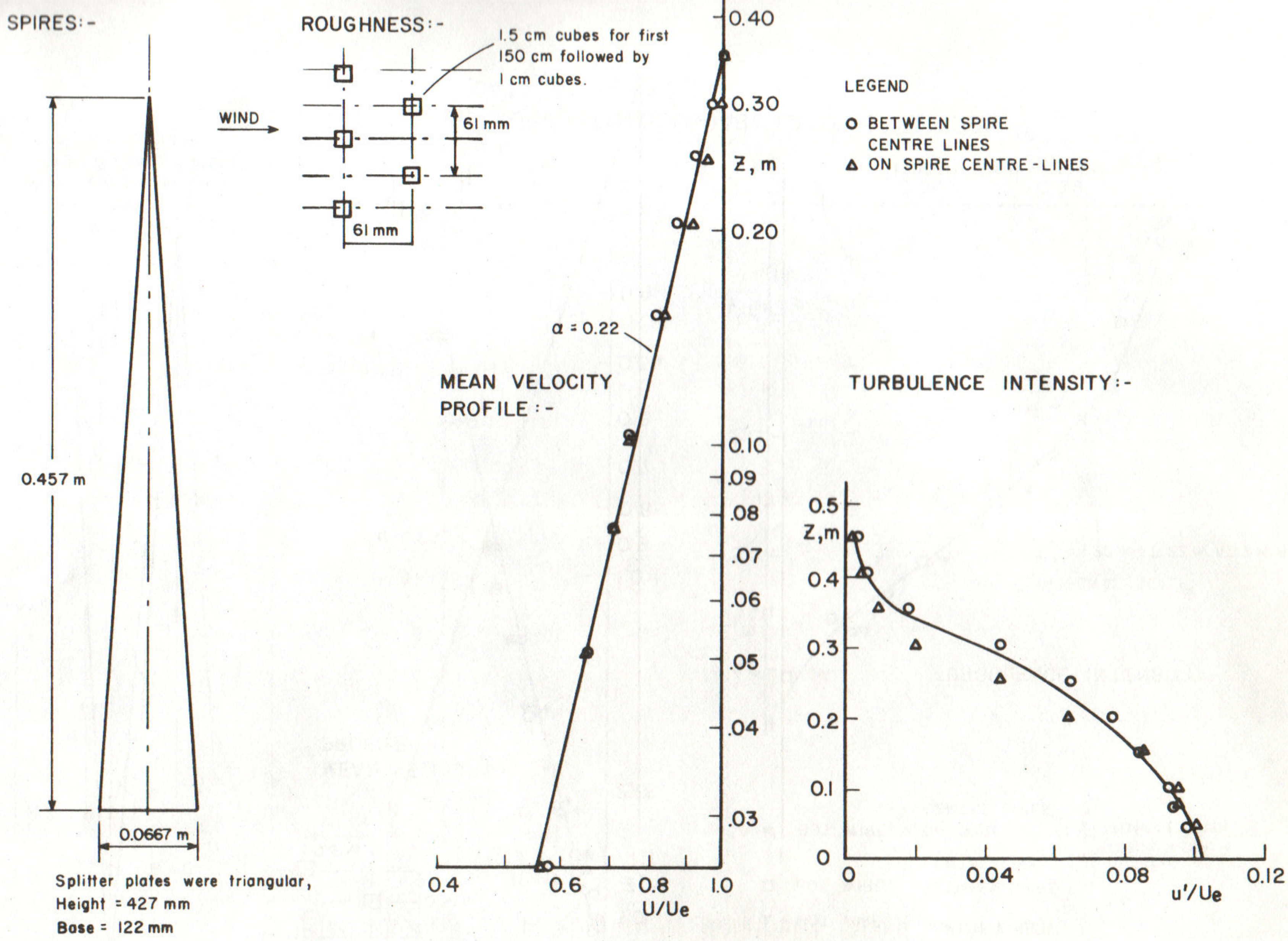

Splitter plates were triangular,
Height = 427 mm
Base = 122 mm

FIG 21 1:1000 SCALE SUBURBAN BOUNDARY LAYER SIMULATION
(UNPUBLISHED WORK IN CONNECTION WITH REF 9) DATA AT $x_o = 4.5$ h

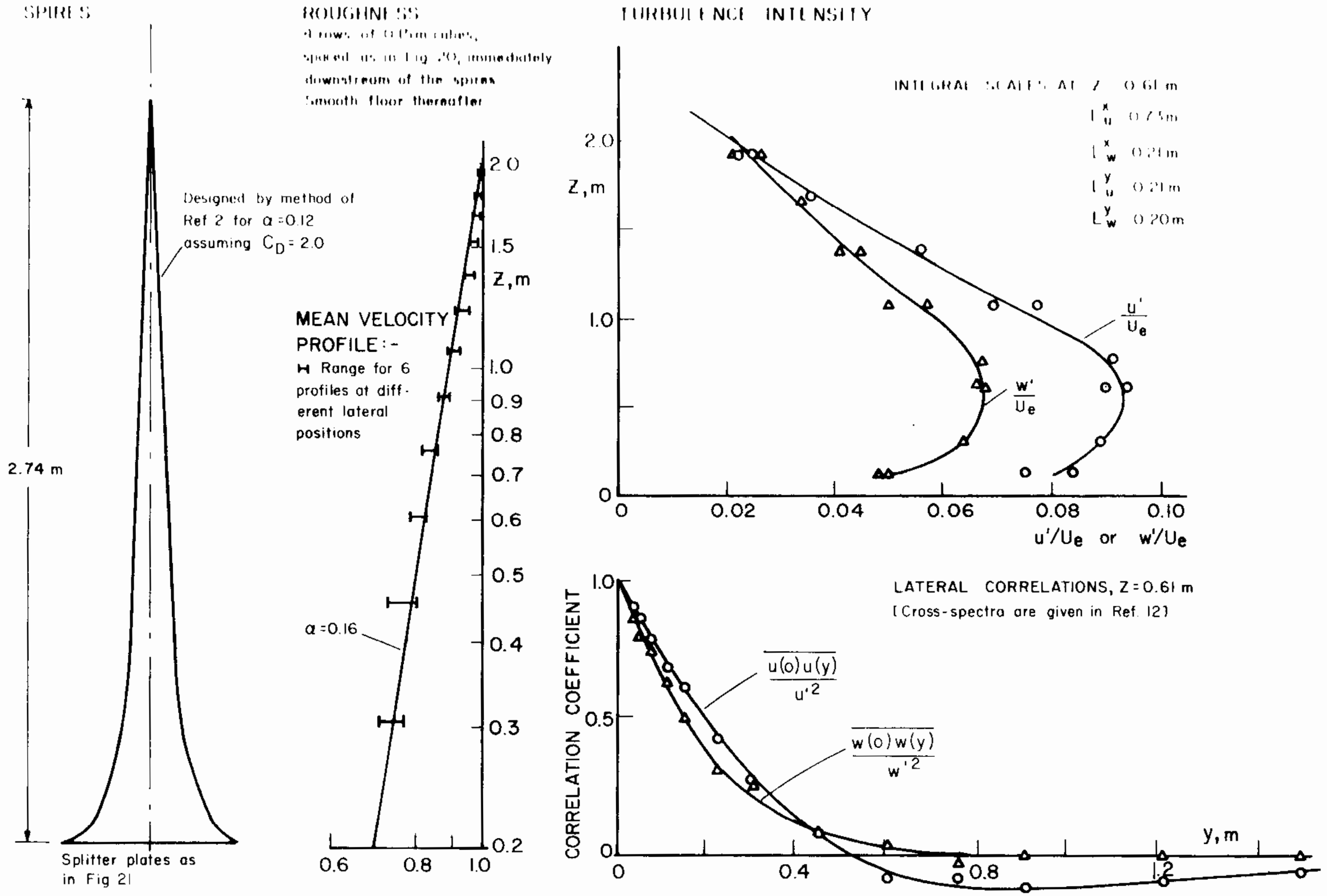

FIG 22 1:110 SCALE SMOOTH FETCH BOUNDARY LAYER SIMULATION(11)
DATA AT X_o = 6h

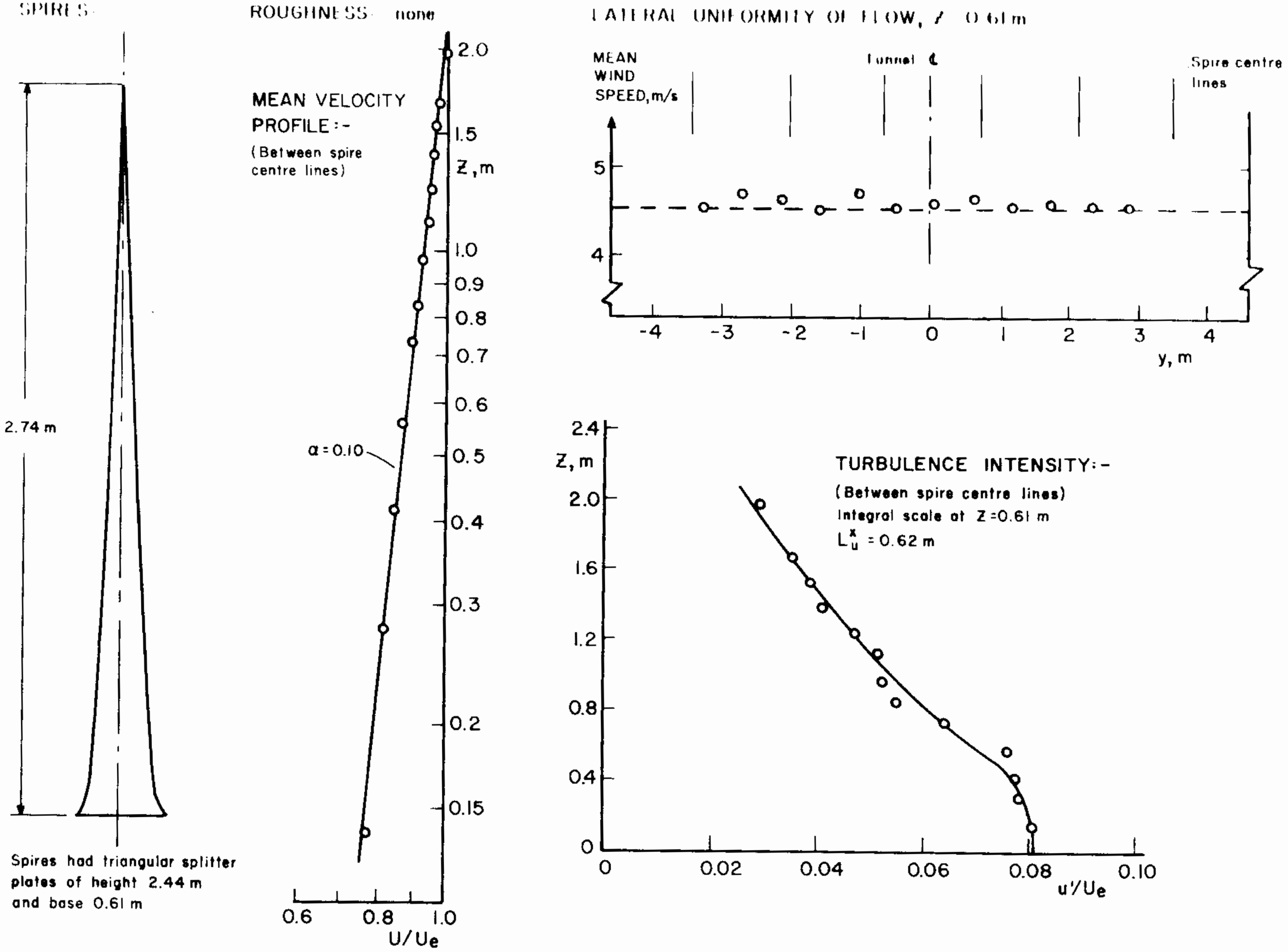

FIG 23 1:110 SCALE VERY SMOOTH FETCH BOUNDARY LAYER SIMULATION$^{(12)}$
DATA AT $x_0 = 6$.

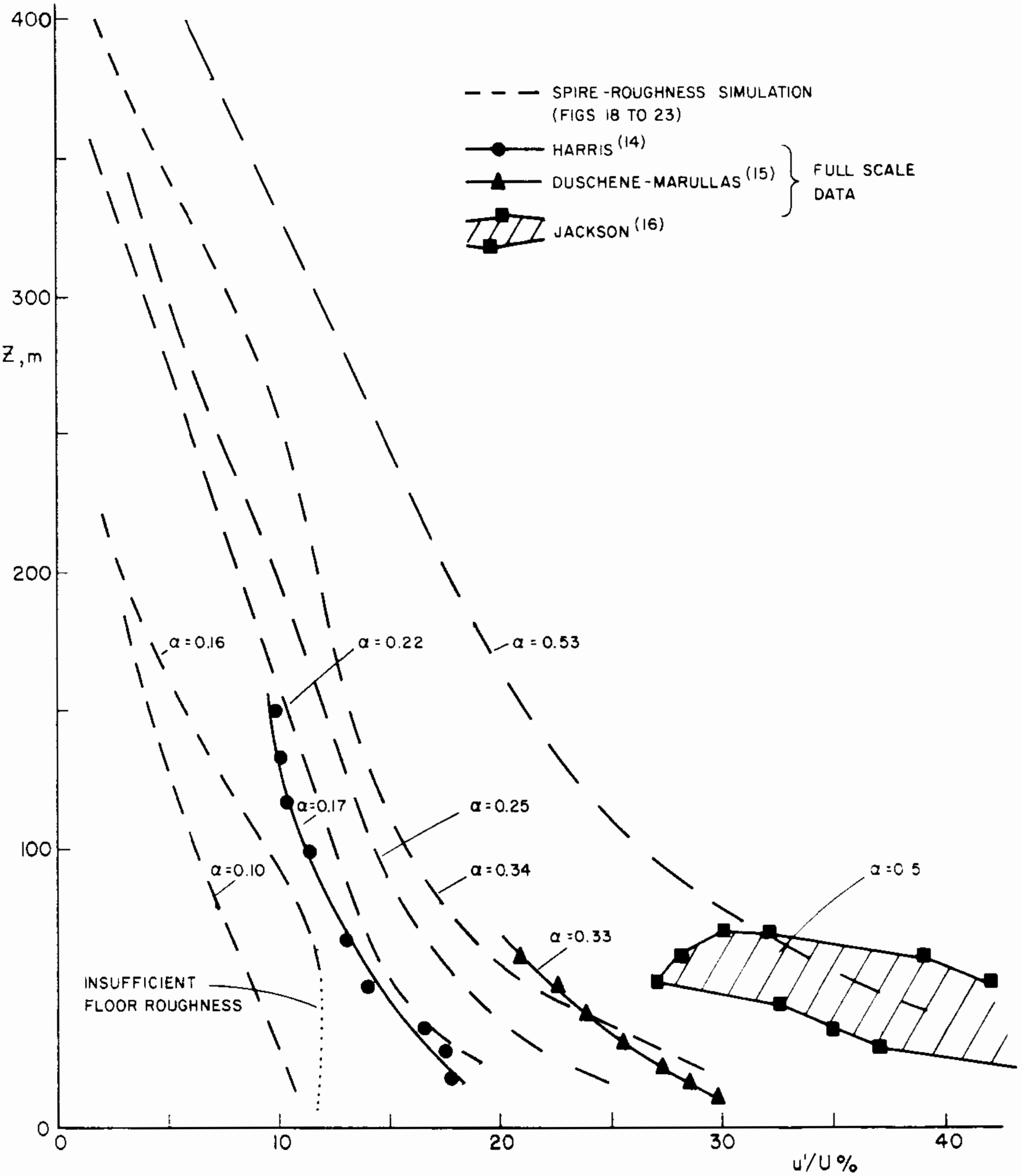

FIG 24 COMPARISON WITH FULL SCALE TURBULENCE INTENSITY BASED ON LOCAL VELOCITY

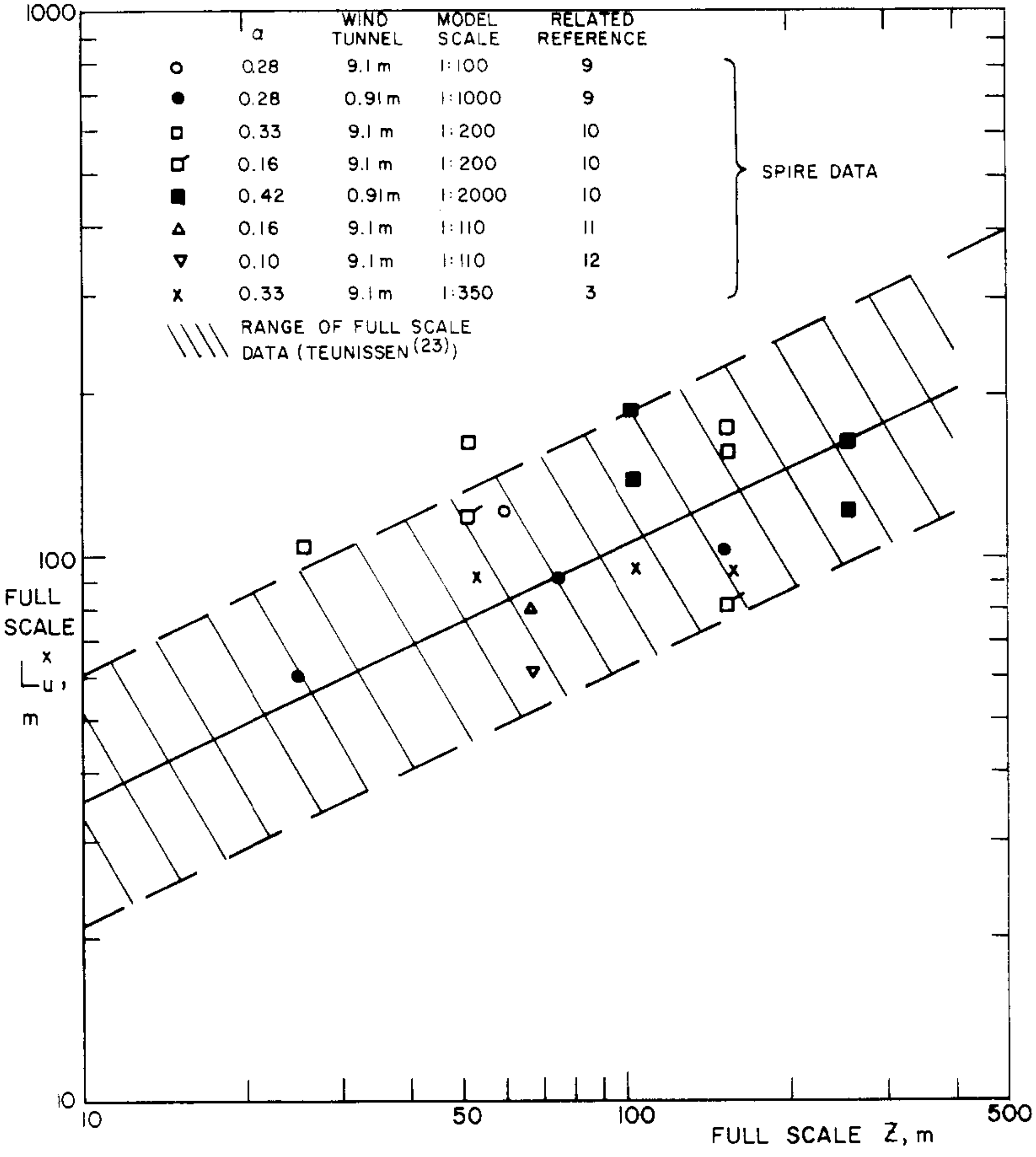

FIG 25 LONGITUDINAL INTEGRAL SCALE OF THE TURBULENCE AS DETERMINED BY THE SPECTRAL FIT METHOD